HAL
open science

The grainsize of volcanic fall deposits: Spatial trends and physical controls

Julia Eychenne, Samantha L Engwell

To cite this version:

Julia Eychenne, Samantha L Engwell. The grainsize of volcanic fall deposits: Spatial trends and physical controls. geological society of america, In press, 10.1130/B36275.1 . hal-03854740v1

HAL Id: hal-03854740

https://uca.hal.science/hal-03854740v1

Submitted on 16 Nov 2022 (v1), last revised 20 Nov 2023 (v2)

HAL is a multi-disciplinary open access archive for the deposit and dissemination of scientific research documents, whether they are published or not. The documents may come from teaching and research institutions in France or abroad, or from public or private research centers.

L'archive ouverte pluridisciplinaire **HAL**, est destinée au dépôt et à la diffusion de documents scientifiques de niveau recherche, publiés ou non, émanant des établissements d'enseignement et de recherche français ou étrangers, des laboratoires publics ou privés.

The grainsize of volcanic fall deposits: Spatial trends and physical controls

Julia Eychenne[1,2,*] and Samantha L. Engwell[3]

[1]*Université Clermont Auvergne, CNRS, IRD, OPGC, Laboratoire Magmas et Volcans, F-63000 Clermont-Ferrand, France*

[2]*Université Clermont Auvergne, CNRS, INSERM, Institut de Génétique Reproduction et Développement, F-63000 Clermont-Ferrand, France*

[3]*British Geological Survey, The Lyell Centre, Edinburgh, UK*

**Corresponding author: julia.eychenne@uca.fr*

Published in 2022 in GSA Bulletin

Science Editor: Brad Singer Associate Editor: Michael Ort

Manuscript Received 6 August 2021

Revised Manuscript Received 15 July 2022

Manuscript Accepted 22 August 2022

Post-print of the reference hereafter:

Eychenne J, Engwell S, 2022. The grainsize of volcanic fall deposits: Spatial trends and physical controls. GSA Bulletin. https://doi.org/10.1130/B36275.1

ABSTRACT

Volcanic tephra fall deposits, which form during explosive eruptions, are commonly characterized in terms of their thickness and grainsize. While significant efforts have been undertaken to relate spatial trends in thickness to plume dispersion processes, comparably few studies have focused on understanding variations in grainsize. Yet, grainsize is a key parameter providing insight into eruption dynamics, from magma fragmentation to plume transport processes, and modulates the impacts of tephra. Here, we present a set of grainsize data extracted from the published record for 56 deposits that represent a range of eruption intensities and magnitudes. We systematically analyze the deposits in terms of modality (bimodal or unimodal grainsize distributions) and provide the median particle diameter with distance from source for component distribution modes. We found that bimodal fall deposits are formed by eruptions with large amounts of fine particles (<100 μm) and that all tephra-fall deposits show characteristic patterns of grainsize decay with distance from source that can be related to eruption plume height and thus intensity. The grainsize decay trends are also related to ash dispersion and deposition processes such as individual particle settling versus collective settling mechanisms. The maximum distance from source reached by particles of different sizes is controlled by a combination of source and transport processes. This data set provides insight into the preservation potential of deposits of different grainsizes at varying distances from their sources. Finally, we emphasize the importance of using grainsize trends in combination with thickness trends to interpret tephra-fall deposit records.

INTRODUCTION

Explosive volcanic eruptions inject great amounts of particles, called tephra, into the atmosphere, which can be transported long distances before they are deposited on the ground, where they create widely dispersed, continuous layers blanketing topography. These tephra-fall deposits generally decrease in thickness and grainsize away from source (Thorarinsson, 1954; Pyle, 1989; Bonadonna et al., 2015c), which enables eruption size to be inferred (i.e., volume, magnitude, and intensity; Pyle, 1989, 1995, 2000; Bonadonna et al., 2015a) and the study of eruption processes (i.e., eruption column dynamics, plume height, explosivity, style; Walker, 1971; Walker, 1973; Carey and Sparks, 1986; Burden et al., 2011; Rossi et al., 2019). In particular, the grainsize of tephra-fall deposits provides information about magma ascent and fragmentation processes (e.g., Alidibirov and Dingwell, 1996; Rust and Cashman, 2011; Dellino et al., 2012; Liu et al., 2015) and the mechanisms of volcanic plume formation, dispersion, and sedimentation through the atmosphere (e.g., Carey and Sigurdsson, 1982; Costa et al., 2010; Girault et al., 2014; Manzella et al., 2015; Del Bello et al., 2017).

The grainsize of fall deposits is generally measured at individual locations by combining mechanical clast sieving and fines-sensitive analytical methods, such as laser diffraction and dynamic image analysis (e.g., using CAMSIZER or MORPHOLOGI G3; Eychenne et al., 2012; Buckland et al., 2021). These individual measurements are often spatially interpolated to obtain the total grainsize distribution (TGSD) of the deposit (Bonadonna and Houghton, 2005; Bonadonna et al., 2015a; Costa et al., 2016; Pioli et al., 2019), which is an estimate of the total particle size distribution within the buoyant convective column before transport fractionation processes occurred. TGSDs are widely used as inputs in numerical models of tephra transport and deposition (Costa et al., 2006; Osman et al., 2020) and to assess mechanisms of magma fragmentation (Rust and Cashman, 2011; Cashman and Scheu, 2015). Trends in maximum grainsize form the basis of a plume ascent model (Carey and Sparks, 1986) updated in Burden et al. (2011) and Rossi et al. (2019) that is still used today to assess the plume height at the vent during explosive eruptions. In addition, numerical models of tephra transport and deposition are overwhelmingly developed and validated using thickness (or mass load) spatial variations (Folch et al., 2010; Beckett et al., 2015; Tadini et al., 2020) with relatively few studies validating model outputs using grainsize (Bonadonna et al., 2002a). The spatial variations of individual grainsize distributions in tephra-fall deposits are underexploited in comparison to other measurements such as deposit thickness.

Characteristic grainsize decays can be observed in several individual fall deposits. For example, the fall deposits from the Campanian Ignimbrite and Minoan eruptions show a decrease in median grainsize away from source before reaching a plateau of constant grainsize at large distances from source (constant grainsize between 950 km and 2300 km from vent in the Campanian Ignimbrite deposit, and 300 km and 500 km in the Minoan deposit; Sparks and Huang, 1980; Engwell et al., 2014). Similar trends were observed in the deposit from the 18 May 1980 Mount St. Helens eruption (Eychenne et al., 2015), and an analysis of published grainsize information for a large number of fall deposits (Engwell and Eychenne, 2016) implies that this is the same for deposits from a wide range of eruption dynamics. In comparison, a recent analysis of several phreatomagmatic deposits shows little change in grainsize with distance from vent (Osman et al., 2020). How these characteristic spatial grainsize trends vary across different eruption types, and how they relate to the fragmentation mechanisms, eruption dynamics, and the transport and deposition processes, are open questions.

Answering these questions would bring valuable new insights into the physics of explosive eruptions (from magma ascent to ejection) and volcanic plumes (from the formation at the vent to the dispersion in the atmosphere). Terms such as "proximal," "medial," and "distal" are commonly used when describing distance from source of volcanic deposits. These terms identify regions close to, intermediate from, and far from vent, respectively, and correspond to different absolute distances for fall deposits from eruptions of different sizes. No objective criteria exist to define proximal, medial, and distal regions, but this gap could be filled by using grainsize trends with distance.

Additionally, documenting how tephra is transported and spatially distributed in different eruption scenarios is key information for mitigating the impacts from tephra fall, such as those on aviation or health. Indeed, aircraft engines are particularly susceptible to ingestion of fine particles (Vasseur et al., 2013; Kueppers et al., 2014), and therefore it is important to understand to what distances such grainsizes are transported. The respiratory hazard for humans during or after eruptions is caused by the poor air quality resulting from the suspension of volcanic particles (Carlsen et al., 2015). Human respiratory systems are particularly susceptible to particles of less than 10 μm, which cause acute health effects (Baxter et al., 1981; Horwell and Baxter, 2006; Baxter et al., 2014). Quantifying the probability of tephra of given sizes reaching given distances in the atmosphere and on the ground is thus critical for these applications.

Finally, a thorough description and classification of grainsize trends in tephra-fall deposits would provide an invaluable tool for refining numerical models of tephra transport and deposition. Indeed, the major challenge with current models relates to the difficulty in reproducing the processes of particle sedimentation in the Earth's complex atmosphere (Watt et al., 2015; Poulidis et al., 2021). Spatial grainsize trends on the ground could be a robust means to test and validate these models. While the decay of grainsize distributions away from vent has been described for many deposits (e.g., Fisher, 1964; Brazier et al., 1983; Sparks et al., 1983; Engwell et al., 2014; Engwell and Eychenne, 2016) and has been related to eruptive plume height and used for eruption classification (Pyle, 1989; Bonadonna and Costa, 2013), these studies typically have focused on a single or small number of eruptions. To fill these gaps in knowledge, we analyzed grainsize information at various distances from vent from several tephra-fall deposits and systematically compiled this information into a self-consistent data set that allows the comparison and classification of fall deposits from eruptions spanning a wide range of magnitudes and intensities. We present characteristic spatial grainsize trends and correlate them with eruption dynamics. Our findings enable description of the heterogeneity of tephra-fall deposits and their spatial variability for different eruption scenarios and provide novel insight into the physical controls on tephra-fall deposit grainsize, from fragmentation to transport processes. They also have important implications for ash transport in distal reaches and the use of tephra-fall deposit records.

DATA SET

This study uses grainsize data and source parameters from 56 tephra-fall deposits from a range of magmatic and phreatomagmatic eruptions (Fig. 1 and Table 1). Grainsize and eruption information was collected from the published record (mostly peer-reviewed publications and some published masters and doctoral theses) and open access volcanological databases (e.g., Global Volcanism Program [Smithsonian Institution, https://volcano.si.edu/], the International Association of Volcanology and Chemistry of the Earth's Interior Commission on Tephra Hazard Modeling [https://thm.iavceivolcano.org/], and the Independent Volcanic Eruption Source Parameter Archive [Aubry et al., 2021]). All references are provided in Table 1 and listed in the Supplemental Material.[1]

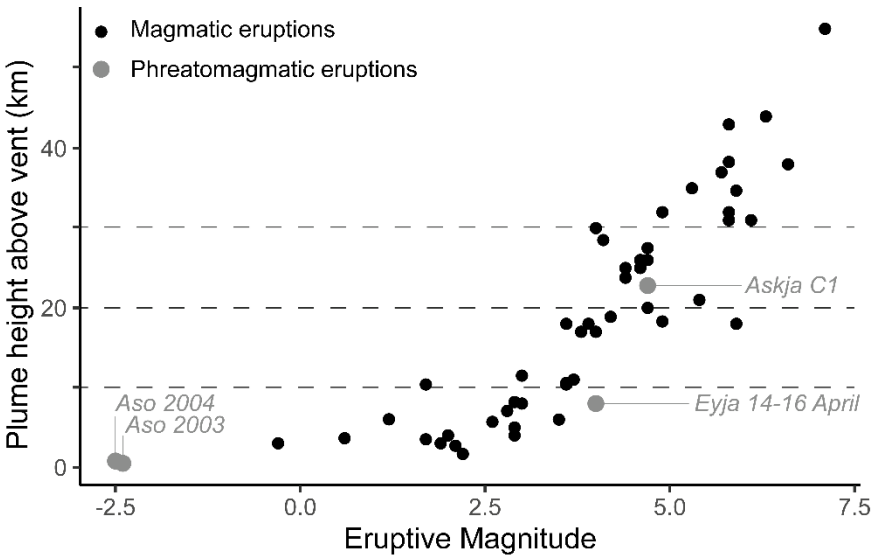

Figure 1. **Maximum column height versus magnitude is plotted for all of the eruptive events compiled in our data sets (Table 1) except for the Hverfjall 2500 B.P. and Reykjanes 1126 CE phreatomagmatic eruptions, for which the plume height is unknown. Phreatomagmatic and magmatic eruptions are in gray and black, respectively. See Table 1 for information on the eruptive events and associated deposits, magnitudes, and plume height values, as well as references.**

Information was collected on the characteristics of each tephra-fall deposit (e.g., stratification, grainsize polymodality, and grainsize measurement method; Table S1 [see footnote 1]). All of the grainsize distributions (GSD) compiled in this study were either unimodal or bimodal. Bimodal distributions have two distinguishable peaks, i.e., two modes. Narrow peaks (often a single phi or half-phi interval, *where phi = –log$_2$ (particle diameter in mm)*) in the coarse lapilli range (>8 mm) are not considered to be modes, as these are found in samples close to vent and most likely were caused by ballistic clasts (see, for example, GSDs from the 13 February 2014 Kelud eruption in Maeno et al., 2019).

Information on each associated eruption was also collected from the published record (Table 1) and includes:
(1) Eruption type, categorizing eruptions as either *magmatic* or *phreatomagmatic*.
(2) Magnitude of tephra-fall deposit, estimated from the mass of the tephra-fall deposit using the relation: $M = log_{10}[erupted\ mass\ (kg)] - 7$ (Pyle, 2000). The deposit mass was either calculated from the deposit volume using a measured or assumed deposit bulk density or directly assessed from isomass maps in the publications (see Table S1).
(3) Maximum column height above vent, typically defined by observations (e.g., webcams, radar, or satellite remote sensing) or by applying empirical methods to deposits such as the model from Carey and Sparks (1986). The method used for each example is given in Table S1, along with the associated references.
(4) Occurrence of pyroclastic density currents (PDC), based on observations made during the eruptions or observations of PDC deposits stratigraphically associated with an eruption.

[1]Supplemental Material. Containing one pdf file with Supplemental Information (Figs. S1–S4 and list of references from Table 1) and 3 Excel spreadsheets (Tables S1–S3). Please visit https://doi.org/10.1130/GSAB.S.21066313 to access the supplemental material, and contact editing@geosociety.org with any questions.

For some eruption parameters, the values inferred in the literature varied among sources, in which case we used an average or a consensual value. In cases where it was not clear whether plume height related to height above vent or sea level, we followed a methodology similar to that defined by Deligne (2021), whereby, for example, plume heights from pilot reports or satellite imagery are assumed to represent height above sea level rather than height above vent.

METHODS

Compiling and Processing Grainsize Information

The grainsize data set (Table S2; see footnote 1) includes the distance from vent (Dist) of individual tephra samples and the median diameter (Md) for each unimodal GSD, or, for bimodal GSDs, the Md of each individual deconvolved subpopulation, as explained below. Md is expressed here in millimeters and was converted from the Mdphi values (Inman, 1952) found in the relevant publications or calculated herein after deconvolution. Md represents the grainsize separating the lowest 50% from the highest 50% of values, and it is inferred graphically from a cumulative density function without assuming any distribution shape. All of the tephra samples compiled here correspond to tephra-fall deposits, i.e., areas where tephra deposition was significant enough to create a deposit identifiable by eye.

Several tephra-fall deposits in our data set are characterized by bimodal GSDs (Fig. S1; see footnote 1). The Md of a bimodal GSD is a poor measure of its characteristics because it does not correlate with the grainsizes of maximum occurrence (represented by the GSD's modes; Fig. S1). The Mds of the two subpopulations extracted from the GSDs by deconvolution define distinct and delimited variation fields. These cannot be identified from the analyses of the GSD Md variations (Fig. S2; see footnote 1), which highlights the lack of resolution of this latter parameter. Hence, in our grainsize data set, unimodal GSDs are described by a single Md, while bimodal GSDs are deconvolved by fitting each observable peak with a subpopulation distribution that is then described by its own Md.

In the published record, grainsize information is presented in various ways. In some sources, raw GSDs are provided as volume or weight probability density functions. They are often presented on phi scales and more rarely on metric scales. In other cases, only distribution statistics (e.g., mode, median, and sorting) are presented, commonly plot against sample location distance from vent. In the case of layered tephra-fall deposits, grainsize data refer in some sources to the complete deposit and in others to individual layers. To build a homogeneous data set and enable direct comparison of eruptions and deposits, we only include GSDs that reflect the whole deposit, including those showing stratification. Stratified deposits are identified in Table S1. While a deposit may exhibit individual units in proximal regions, it is often impossible to distinguish different units in distal deposits, which likely represent either the most intense phase of the eruption or a contribution from multiple eruption phases, including both Plinian and co-PDC contributions. We used published Md values or calculated Md values from available GSDs. Published Md values were only used if evidence for the unimodality of the GSD was provided or if they referred to deconvolved subpopulations of bimodal GSDs. It is important to note that due to the criteria used, some of the grainsize information existing in the published record were not included in our data set.

The grainsize data compiled here were acquired by combining sieving in the coarse range (roughly coarser than 100 μm, but this varies among studies) and a variety of different measurement methods in the fine range. The grainsize analytical methods for each of the 56 eruptions in our data set are indicated in Table S2. These methods include (1) laser diffraction, based on the principle of light scattering (using instruments such as the Malvern Mastersizer or Beckmann Coulter); (2) sedimentation, based on the assessment of the particle size from the settling velocity using Stokes' law (pipette method, Sedigraph instrument); (3) electrosensing zone, based on the resistive pulse sensing in an electrical field (using instruments such as the Elzone Celloscope); and (4) dynamic image analyses, based on image acquisition and analyses of the particles dispersed in a flowing fluid

(using instruments such as the Camsizer). Different measurement techniques can produce various grainsize distributions for a given sample (Buckland et al., 2021), which could explain some of the differences in grainsize among the tephra-fall deposits compiled here.

Deconvolution of Bimodal Grainsize Distributions

Raw bimodal GSDs were deconvolved using the fully automated DECOLOG software (Bellotti et al., 2010; Caballero et al., 2014), which uses an iterative algorithm for nonlinear fitting of log normal or Weibull functions. Following the approach described in Eychenne et al. (2015), only peaks with an overlap smaller than ~70% were deconvolved into individual subpopulations to avoid inaccurate deconvolution results. The deconvolution methods used in the publications from which we extracted pre-deconvolved Md values included (Table S2) software-based DECOLOG, SFT (Wohletz et al., 1989), and LOGN2D (Eychenne et al., 2012), as well as hand-fitting (Brazier et al., 1983). We hereafter refer to the two subpopulations extracted from the bimodal distributions as "coarse" and "fine."

RESULT OF THE GRAINSIZE ANALYSIS

Characteristics of the Eruptions in the Data Set

The 56 tephra-fall deposits in our data set (Table 1) were generated by magmatic and phreatomagmatic eruptions with a wide range of plume heights and magnitudes (Fig. 1). The plume height is a measure of the intensity of an eruption, i.e., the rate at which material is erupted (Pyle, 2000; Mastin et al., 2009). The magnitude refers to the total amount of material erupted (Pyle, 2000), and hence represents a measure of eruption size. There is a positive correlation between the amount of material erupted during an explosive eruption and the rate at which it is erupted (Carey and Sigurdsson, 1989; Pyle, 2000), as illustrated by the correlation between plume height and magnitude in our data set (Fig. 1). The deposit data set compiled here spans a representative range of magmatic eruptions, from low to high intensities and magnitudes. Only six eruptions in the data set are phreatomagmatic, but they span a comprehensive range of eruption intensities and magnitudes.

Different numbers of grainsize distributions from individual locations are available for each eruption. The number of data points, and the minimum and maximum distances from source at which these data points were collected for each eruption, are reported in Table S1. In general, eruptions with lower plume heights have more grainsize information closer to source, while for the largest eruptions, more data are available at large distances from vent.

Categories of Tephra-Fall Deposits

The 56 tephra-fall deposits analyzed here (Table 1 and Fig. S3; see footnote 1) can be grouped into distinctive categories based on their grainsize characteristics. Some deposits, hereafter referred to as *unimodal deposits*, are characterized by unimodal GSDs across the deposit extent (Fig. 2A) or are dominated by unimodal GSDs with rare bimodal GSDs at scattered locations (Fig. 2B). The boundary between unimodal deposits with and without scattered bimodal GSDs is indistinct; some deposits classified as unimodal here include subordinate bimodal samples that were disregarded due to the lack of raw data for deconvolution (e.g., the 1104, 1300, 1693, and 1766 Hekla eruptions; Janebo et al., 2018). Other deposits, hereafter referred to as *bimodal deposits*, are characterized by bimodal grainsize distributions throughout (Fig. 2C) or are dominated by bimodal GSDs but also show unimodal GSDs at distal locations (Fig. 2D).

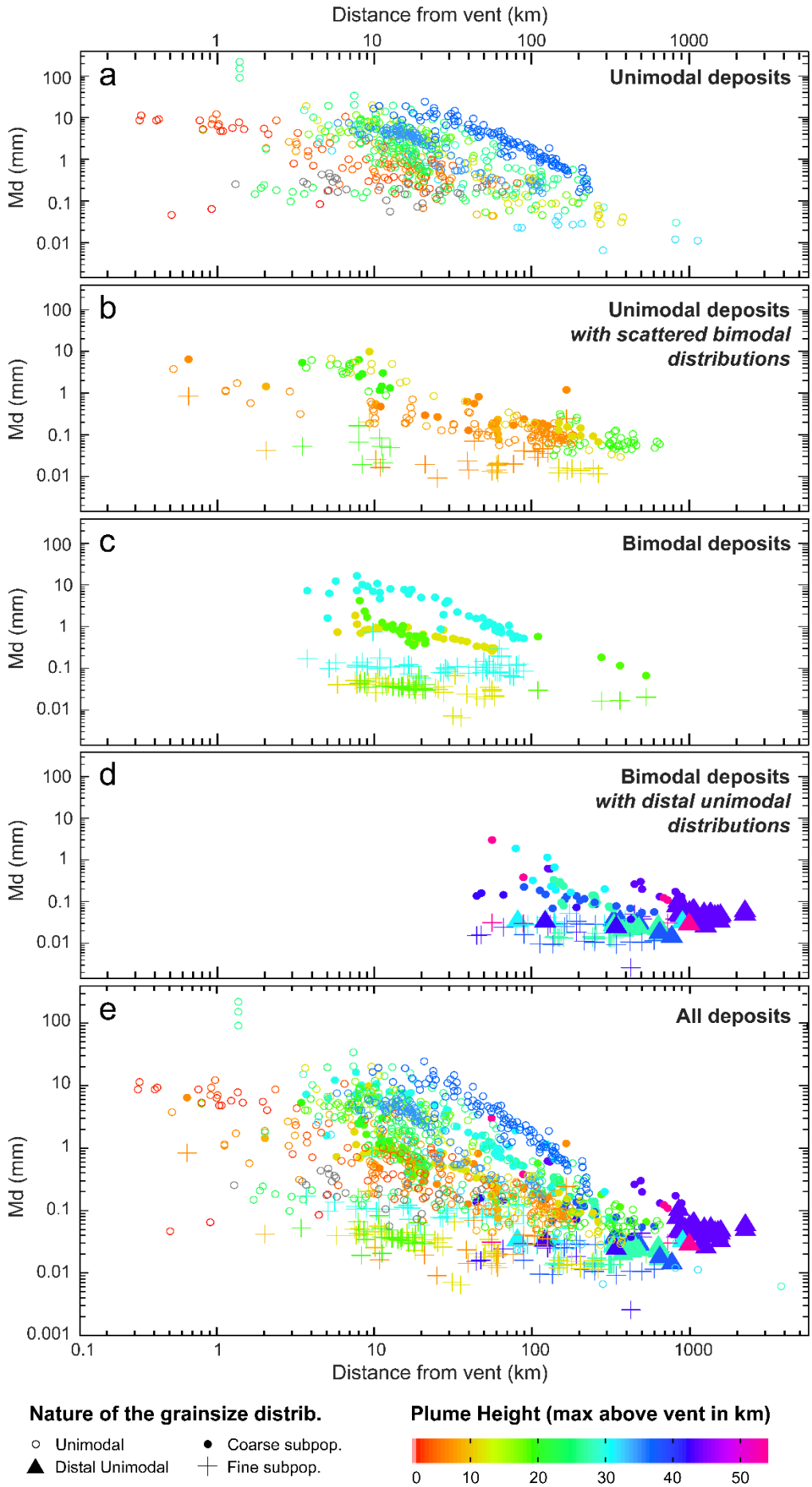

Figure 2. **Variations in median diameter (Md) of the grainsize distributions (GSDs) are plotted with the distance from vent for the four categories of tephra-fall deposits identifiable in our data set (Table 1): (A) unimodal, (B) unimodal with scattered bimodal distributions, (C) bimodal, (D) bimodal with distal unimodal distributions, and (E) all deposits. Symbols are used to distinguish Md values from unimodal GSDs (open circles), coarse subpopulations (filled circles), fine subpopulations (crosses), as well as distal unimodal GSDs (triangles). The data points are colored according to the maximum plume height above vent (column height) using a continuous color scale.**

Both types of bimodal deposits show converging grainsize subpopulations with distance from vent that eventually merge in distal reaches and contribute to the distal unimodal GSDs (Fig. S1). The two categories of bimodal deposits probably represent a single category, assuming that bimodal deposits without unimodal GSDs at distal locations were not sampled at distances great enough to identify where the GSDs become unimodal.

Unimodal deposits are formed by a wide range of eruptions with low to high plume heights (<1– 37 km; Fig. 2A). They also span a wide range of eruption magnitudes (0–5.9; Table 1). Unimodal deposits with scattered bimodal distributions were found for low to intermediate plume heights (5–18 km above vent; Fig. 2B) and magnitudes (~2–4; Table 1). Bimodal deposits were found for intermediate to high plume heights (11–30 km above vent; Fig. 2C) and magnitudes (1.7–5.9; Table 1). Bimodal deposits with distal unimodal distributions were found for high plume heights (>27 km above vent; Fig. 2D) and magnitudes (>4.7; Table 1).

Downwind Grainsize Variations

When examining the spatial variations of the grainsize data in a log–log space where Md and distance are both expressed in metric units, we identified three distinctive grainsize trends across all of the deposit categories (Figs. 2 and 3). A *coarse trend*, showing a clear decrease in Md with distance from vent, is defined by the unimodal GSDs and the coarse subpopulations of the bimodal GSDs (open and filled circles in Figs. 2 and 3). A *fine trend*, showing little change in Md with distance from vent, is defined by the fine subpopulations of bimodal GSDs (crosses in Figs. 2 and 3). Finally, a *unimodal distal trend* was defined that often follows the same end as the fine trend where present, and that is restricted to large distances from vent, and shows little change in Md with distance (triangles in Figs. 2 and 3). Within each individual deposit (Fig. 3), a range in Md is observed at constant distances from vent, which represents the crosswind changes in grainsize. Despite this scatter, the coarse, fine, and distal unimodal trends have distinctive characteristics that can be interpreted in terms of downwind variations.

The coarse trend spans a wide range of Md values, from 200 mm to 6 μm, and shows a general decrease in Md with distance from source at a rate correlated with the eruption plume height (Fig. 2E). This correlation is valid for magmatic eruptions only. The deposits from phreatomagmatic eruptions follow a different pattern and show little grainsize change with distance (Figs. 3 and 4). This has been demonstrated using a compilation of bulk (i.e., non-deconvolved) grainsize data (Osman et al., 2020). Within a given range in plume height (Fig. 4), magmatic eruptions display decay trends that reach Md values of 100 μm at increasing distances from vent with increasing plume heights (Fig. 3). This means that at a given distance from vent, tephra-fall deposits show decreasing Md values (on average) with decreasing plume height, which is well demonstrated by the boxplots in Figure 4. Most deposits from eruptions with plume heights between 0 km and 10 km are unimodal, with Md grouping along a similar trend with distance from source (Fig. 3D). While there are more bimodal deposits for eruptions with plume heights of 10–20 km and 20–30 km, the unimodal Md and coarse Md again show similar decay trends with distance from source (Figs. 3B and 3C). For eruptions with plume heights of >30 km above vent, two parallel coarse trends with similar decay rates are distinguishable (Fig. 3A). The upper trend is described by the Md data from the Taupo deposit at distances of <200 km from vent and the Campanian and Mazama deposits at distances of >500 km from vent. In this upper trend, Md values of 100 μm are observed ~800 km from vent (Fig. 3A). The lower trend consists of the Md data from the Rungwe and Huaynaputinia eruptions at distances of <100 km from vent and the Pinatubo, Minoan, and Tambora eruptions at distances of >100 km from vent. In this lower trend, Md values of 100 μm are observed ~400 km from vent (Fig. 3A). In most deposits for each plume-height category, we observe that the coarse trend reaches a plateau in Md distally, where Md remains constant with distance from vent around a grainsize value that varies among plume height categories (Fig. 3). These results indicate that at a given distance from source, the median grainsize in the coarse trend is correlated with the type (magmatic versus phreatomagmatic) and the intensity of the eruption, with coarser deposits at a given distance resulting from higher intensity magmatic eruptions. This behavior is less obvious (1) at very proximal distances from vent (<10 km), where we observe some overlap among magmatic deposits (Fig. 4), which highlights that a wide range of eruptions can deposit particles of

similar grainsize at such close distances from vent, and (2) for eruptions with plume heights of >30 km above vent, which deposit a wide range of grainsizes at a given distance (see the wider boxplots for this plume height category in Fig. 4).

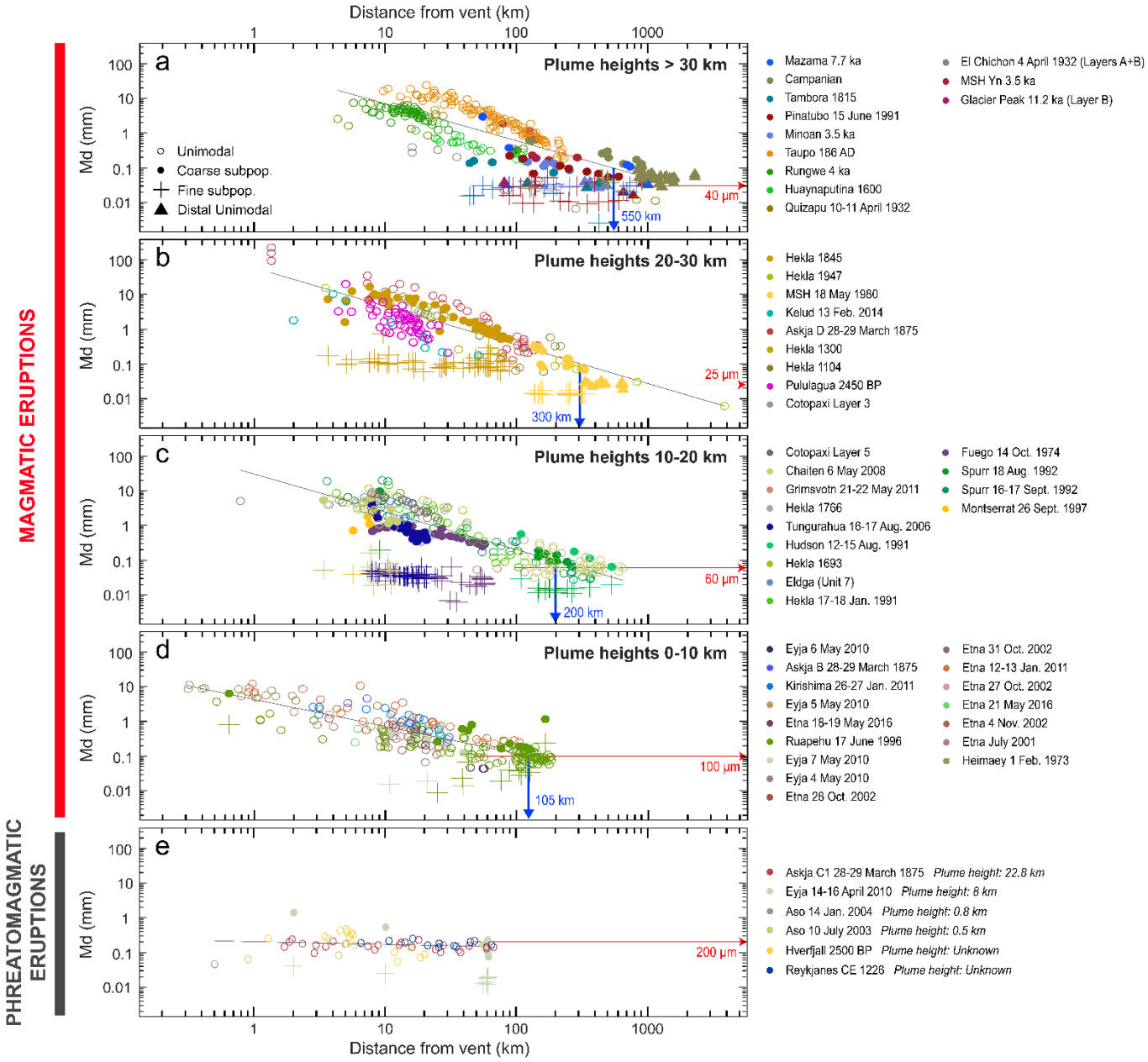

Figure 3. **Variations in median diameter (Md) of the grainsize distributions (GSDs) are plotted with distance from vent for the (A–D) magmatic and (E) phreatomagmatic eruption deposits compiled in our data set. Magmatic eruptions are plotted separately based on the maximum plume heights above vent: eruptions with plume heights above vent (A) >30 km, (B) between 20 km and 30 km, (C) between 10 km and 20 km, and (D) between 0 km and 10 km. The data points are colored by deposit/eruptive event (see Table 1 for more information on the eruptions and references for the plume heights reported here) and ordered in the legend by decreasing plume heights. Symbols are used to distinguish Md values from unimodal GSDs (open circles), coarse subpopulations (filled circles), fine subpopulations (crosses), as well as distal unimodal GSDs (triangles). The gray lines represent the best fit through the coarse trend of deposits grouped by plume heights and magmatic versus phreatomagmatic eruptions. The blue arrows represent the distance from vent at which the best fit lines reach 100 µm. The red arrows highlight the grainsize at which the coarse and distal trends reach a plateau in Md distally.**

The fine trend spans a narrow range of Md values, from 200 μm to 2 μm (except for two values between 700 μm and 800 μm), and shows a very shallow decrease in Md with distance from source (Figs. 2 and 3). Two subparallel trends are apparent (Figs. 2E and 4). The coarsest trend mostly includes the fine subpopulations of the bimodal deposit from the Plinian 1845 Hekla eruption (Fig. 3B), which remains constant with distance with an Md value of 100 μm. The finest trend (<63 μm) mostly includes deposits from eruptions with high intensities (plume heights of >10 km). A slight decrease in Md in this trend is most apparent at distances of 10–100 km from vent (Figs. 2 and 4), while at distances of >100 km from vent, very little change in the fine trend of Md can be observed, with Mds of between 10 μm and 40 μm (Fig. 4 and Table S1).

The distal unimodal trend, mostly seen in deposits from eruptions with plume heights of >30 km (except for the 18 May 1980 Mount St. Helens eruption, whose plume height was between 20 km and 30 km above vent, Fig. 3B), spans a narrow range of Md values, from 100 μm to 15 μm, and shows little variation with distance from source (Fig. 2D).

A common pattern can be identified in the downwind variations of the grainsize: the steep decay of the coarse trend and the shallow decay of the fine trend meet in distal areas, where the distal unimodal trend is found (Figs. 2–4). The fine trend meets the distal unimodal and coarse trends between 500 km and 1000 km from vent (Figs. 2 and 3). The convergence in modes with distance from vent has been identified in some tephra-fall deposits from ignimbrite-forming eruptions (Sparks and Huang, 1980; Brazier et al., 1983; Sparks et al., 1983; Engwell et al., 2014) and from lower intensity eruptions (Eychenne et al., 2012, 2015; Engwell and Eychenne, 2016). Based on the data compiled here, we demonstrate that the spatial variation patterns of the coarse and fine subpopulations follow universal behavior.

What Grainsizes Go Where?

Examining the distribution of Md at various intervals from source (Fig. 4 and Table S3) allows identification of spatial variation patterns among tephra-fall deposits. Because we are analyzing Md sizes, i.e., the median of the size distribution of grains at a given location, our data cannot be interpreted in terms of maximum grainsize transported. In fact, both coarser and finer material are present in the tephra samples. Given that we are working on deconvolved GSDs, we can be confident that the Md refers to a unique mode of the distribution and that the Md values are robust proxies of the most frequent grainsize found at the sampled locations.

Up to distances of 100 km from vent (Fig. 4), the Mds of the GSDs observed in fall deposits range from lapilli (64–2 mm) to fine ash sizes (<63 μm). At 50–100 km from vent, only eruptions with plume heights of >30 km above vent still deposit particles of lapilli-sized Md. Eruptions with lower plume heights deposit particles in the ash-sized range. Further than 100 km from vent, the deposits have an ash-sized Md ranging from coarse (2 mm to 63 μm) to fine ash (<63 μm). Interestingly, fine ash is deposited at all distances from vent for most eruption intensities (Fig. 4). At distances of <10 km from vent, only deposits from eruptions with the greatest plume heights (>30 km) lack fine subpopulations and hence a fine trend (Fig. 4). This reflects a lack of proximal measurements for these examples in our data set rather than an absence of bimodal deposits within this category at these distances.

The data presented here relate to distinct deposits that are identifiable by eye and do not include more diffuse deposits that can only be sampled as cryptotephra (Ponomareva et al., 2015; Stevenson et al., 2015; Cashman and Rust, 2020). However, the information can be used to inform the distances at which identifiable deposits occur for different eruption types (Fig. 4), similar to results using deposit thickness in Mahony et al. (2016). At distances of >500 km from vent, some grainsize information exists for eruptions with plume heights of >10 km above vent, but mostly for eruptions with plume heights of >30 km (Fig. 4). Eruptions with intermediate plume heights tend to have grainsize data extending to distances between 200 km and 500 km from vent (Fig. 4). Eruptions with smaller plume heights tend to show observable deposits to a maximum distance of 200 km from vent (Fig. 4). These distances could be inferred to represent the locations at which distinct ash clouds are

present in the atmosphere; however, particles are likely to travel as dilute clouds farther than the maximum distances inferred here and are deposited as cryptotephra (Cashman and Rust, 2020; Gouhier et al., 2019).

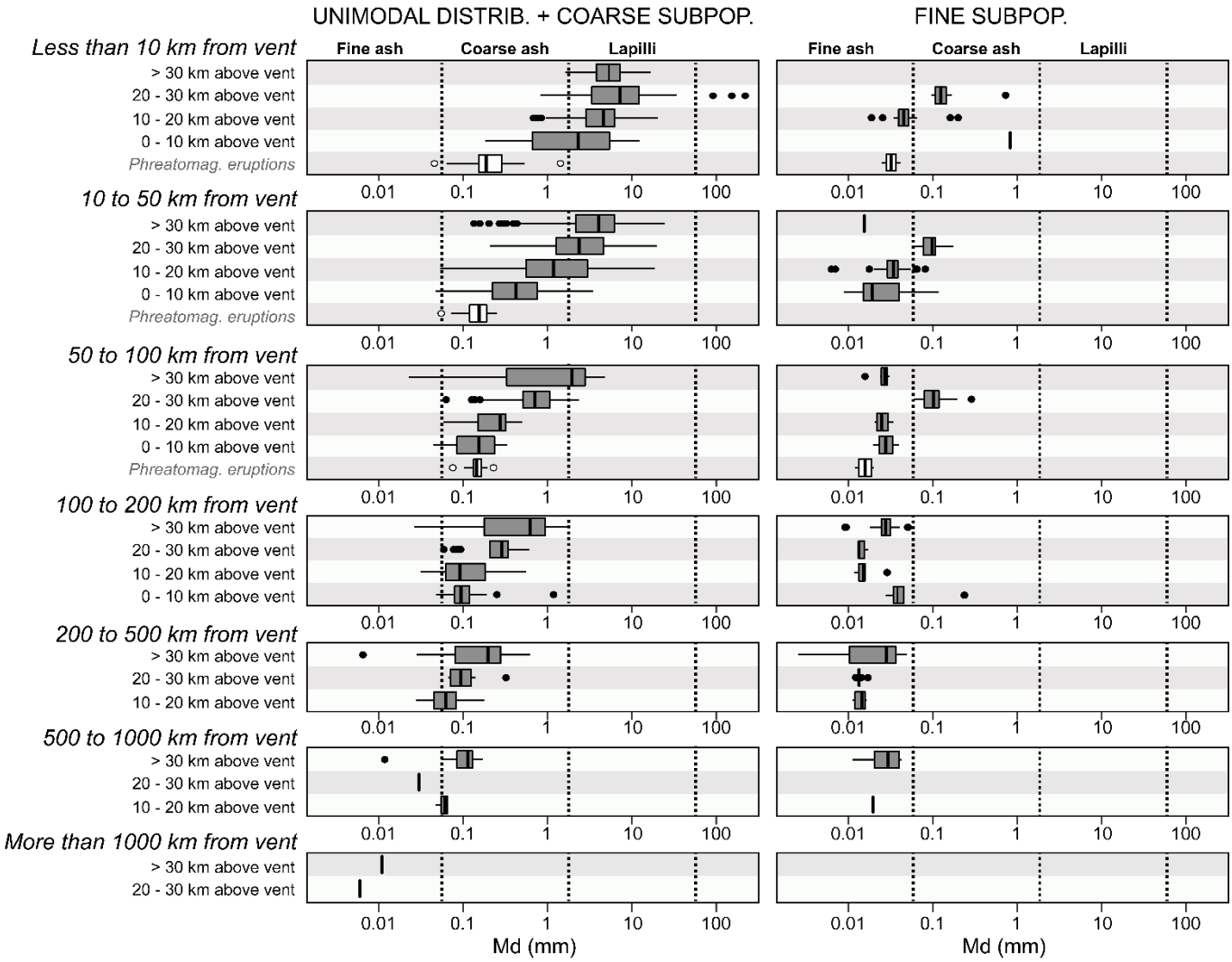

Figure 4. **Plots show distributions of median diameter (Md) in the coarse and fine trends as a function of distance from vent (horizontal panels) and maximum plume height above vent for magmatic eruptions. The coarse trend is defined by the unimodal GSDs excluding the distal unimodal ones, and coarse subpopulations. The fine trend is defined by the fine subpopulations. The phreatomagmatic eruptions are counted separately and represented by white boxplots. The distributions are represented by Tukey whiskers plots, where the thick middle line is the median, and the box spans the interquartile range (25th and 75th percentiles). The lower and upper whiskers show the smallest and largest values no farther than 1.5 × the interquartile range (i.e., distance between the first and third quartiles). Outliers are plotted individually. Statistical parameters are summarized in Table S3 (see footnote 1).**

DISCUSSION

Origin of the Bimodality in Tephra-Fall Deposits

Our work indicates that two main categories of tephra-fall deposits exist: those dominated by unimodal GSDs and those dominated by bimodal GSDs (Fig. 2). Our analysis shows that deposits dominated by bimodal GSDs are from high-intensity eruptions (plume heights of >10 km, Figs. 2C and 2D), while deposits dominated by unimodal GSDs occur for awide range of eruption intensities (Figs. 2A and 2B). The absence of bimodality, and

hence fine subpopulations, in deposits from low-intensity eruptions (plume heights of <10 km; Table 1) can be attributed to the small amounts of fine ash produced by these eruptions. In our data set, these eruptions are typically lava-fountaining in type and therefore have low fragmentation efficiency (Rust and Cashman, 2011). Most phreatomagmatic deposits are unimodal in our data set (Fig. 3E), but this is not universal behavior. Other phreatomagmatic deposits from high-intensity eruptions that are not included here show evidence of bimodality (e.g., Tierra Blanca Joven, El Salvador [Pedrazzi et al., 2019]; Taupo Hatepe, New-Zealand [Walker, 1981]; and Soufriere St. Vincent, 1979 [Brazier et al., 1982]). We can thus conclude that there is no relation between the unimodality or bimodality of a tephra-fall deposit and the involvement of water in the fragmentation process.

Our analyses shows that high-intensity eruptions, which have high fragmentation efficiencies and thus the potential to produce fine, ash-rich plumes, can form both deposits dominated by unimodal GSDs and deposits dominated by bimodal GSDs. This demonstrates that the bimodality of fall deposits is not solely caused by source processes and that transport and deposition processes also play an important role. Previously, the presence of a prevalent fine grainsize subpopulation in tephra-fall deposits has been related to a contribution of fine ash from co-pyroclastic density current plumes (co-PDC, i.e., plumes generated by the lift-off of PDCs during their emplacement). Evidence for such processes has been observed (1) in detailed sedimentological studies of individual tephra-fall deposits (e.g., Campanian ignimbrite, Minoan ignimbrite, 800 yr B.P. Quilotoa, 1974 Fuego, 1980 Mount St. Helens, 2006 Tungurahua; Sparks and Huang, 1980; Di Muro et al., 2008; Rose et al., 2008; Eychenne et al., 2012; Engwell et al., 2014; Eychenne et al., 2015), (2) as well as in a compilation of numerous deposits for which there is record of co-PDC plume formation (Engwell and Eychenne, 2016). This relation was demonstrated based on the comparison between the grainsize of distinct co-PDC deposits and the fine subpopulation of bimodal GSDs, as well as the geometry of the bimodal fallout deposits and the spatial prevalence of the fine subpopulation (Engwell and Eychenne, 2016). However, several of the tephra-fall deposits dominated by bimodal GSDs analyzed in this study are not thought to be associated with PDCs (Fig. S3 and Table S2), namely the 1845 Plinian Hekla eruption (Gudnason et al., 2018) and the 1991 Plinian Cerro Hudson eruption (Scasso et al., 1994). Other potential fine ash contributors to fall deposits that have been invoked to explain bimodality (Gudnason et al., 2018; Janebo et al., 2018), are (1) fine ash from waning or ash-venting eruption phases, which have lower energy and disperse tephra at low altitudes, hence depositing fine ash at the same distances from vent as coarser material from the climatic phase, and (2) syn- and post-eruptive wind remobilization of the contemporaneous fallout deposits, which is a size-selective process responsible for the resuspension and redistribution of fine ash only (Liu et al., 2014). Another potential process of fine ash enrichment of fall deposits is related to the late settling of co-Plinian ash. This term was first defined by Fierstein and Hildreth (1992) in the context of the multiple episodes of the 1912 Plinian Novarupta eruption. Fierstein and Hildreth (1992) describe fine ash that remains aloft after energetic Plinian phases, due to their low terminal velocities, and ends up mixed in with the deposits of subsequent explosive phases. Using the change in magma chemistry that occurred during the eruption, they demonstrated that as much as 4.5% and 12.5% of the fallout volume from the first, largely unimodal, Plinian rhyolitic episode was found in the dacitic fallouts from the second and third Plinian episodes, respectively, which both show bimodality (Fierstein and Hildreth, 1992). Mixing of co-Plinian and co-PDC ash was also proposed to explain the fine contribution in the 800 yr B.P. Quilotoa and Campanian Ignimbrite tephra-fall deposits (Perrotta and Scarpati, 2003; Di Muro et al., 2008), which both have marked bimodality.

Bimodality of fall deposits can also be explained by some mechanisms that enhance the deposition of fine ash in proximal to medial locations. In fact, this is the most commonly invoked process to interpret tephra-fall deposits dominated by bimodality or the occurrence of bimodal GSDs in deposits otherwise dominated by unimodal GSDs (e.g., Carey and Sigurdsson, 1982; Brazier et al., 1983; Bonadonna et al., 2002b, 2011; Gudnason et al., 2017). Such enhanced deposition mechanisms include (1) ash aggregation (Brown et al., 2012), by which small particles cluster together to form a bigger grain with higher settling velocity (Carey and Sigurdsson, 1982), or small particles coat coarser grains and are thus scavenged from the plume (Bagheri et al., 2016), or

hydrometeors induce particle aggregation and settling (Durant et al., 2009; Van Eaton et al., 2015; Gudnason et al., 2017); (2) en-masse settling due to gravitational instabilities (Carazzo and Jellinek, 2013; Manzella et al., 2015); and (3) fine ash entrainment in the tail of bigger grains by a process called wake capture (Lovell and Rose, 1991). All of these processes will be discussed in the next section in relation to the grainsize trends, but they are most prominent in high-concentration plumes. During the 18 May 1980 Mount St. Helens eruption, which produced a strongly bimodal deposit, coarse and fine ash were documented falling concomitantly by syn-eruptive time series sampling, which led to bimodal grainsizes (Scheidegger et al., 1982). Ash clusters were also observed and sampled syn-eruptively for the first time (Sorem, 1982).

Another well-known process that creates polymodality in tephra deposits is a change in wind direction during eruptions. The resulting shift in the plume dispersal axis generates a shift in the tephra depositional axis, leading to overlapping particle sizes on the ground. Such a process was well described during the 2008 long-lasting eruption of Chaiten (Watt et al., 2009) and is generally accompanied by multi-lobate fall deposits.

This grainsize compilation suggests that both a high fine ash content and enhanced deposition processes are prerequisite conditions for generating deposits dominated by bimodality, while deposits dominated by unimodal GSDs but displaying scattered subordinate bimodal samples could solely result from enhanced fine ash deposition without requiring an additional source of fine ash. For example, the 17 June 1996 Ruapehu eruption (Table 1, Fig. 3) generated several bimodal samples despite the deposit being dominated by unimodal GSDs and produced less than 5 wt% of fine ash as inferred from one of the most comprehensive TGSD reconstructions in the literature (Bonadonna and Houghton, 2005). The data presented here show that the Ruapehu grainsize decay plateaus around 100 μm in distal areas (>100 km from vent; Fig. 3D), which confirms that a small amount of fine ash was available during this eruption. On the contrary, all of the deposits dominated by bimodality in our data set were generated by eruptions for which prominent secondary sources of fine ash exist (Table S2). Even the 1845 Hekla and the 1991 Cerro Hudson deposits (Figs. 3B and 3C), which are not considered to be associated with large PDCs and therefore are not enriched by co-PDC ash, have other secondary sources of fine ash. In the case of the 1845 Hekla event, witness accounts describe late settling of fine particles (Gudnason et al., 2018), which could be related to the settling of co-Plinian ash or ash from a waning or ash-venting phase after the main Plinian event. Additionally, wind erosion and remobilization of the tephra-fall deposit were also described after this event (Gudnason et al., 2018). In the case of the 1991 Cerro Hudson eruption, consistently strong winds, combined with pulsatory eruptive activity (Scasso et al., 1994), promoted the mixing of co-Plinian ash with tephra from succeeding phases.

Physical Controls on the Spatial Grainsize Trends

Our work highlights two major findings: (1) all of the tephra-fall deposits contribute to two distinct trends of grainsize decay, coarse and fine, which converge in distal regions where they reach similar grainsizes (Figs. 2 and 3), and (2) a relation exists between the patterns of grainsize decay in the coarse trend and the eruption intensity (plume height; Fig. 4). Here, we discuss the physical controls on these two main results.

Controls on the Coarse and Fine Trends: Differences in Sedimentation Behavior

The steep grainsize decay with distance from vent in the coarse trend, and the shallow grainsize decay in the fine trend (and the phreatomagmatic deposits), are related to the contrasting settling mechanisms controlling the sedimentation of coarse and fine particles. The coarse decay is well explained in the literature by individual particle settling at terminal fall velocity using different physical models (e.g., Walker et al., 1971; Brazier et al., 1982; Carey and Sigurdsson, 1986; Carey and Sparks, 1986; Sparks et al., 1992; Rose, 1993; Eychenne et al., 2017). Based on the thickness trends with distance, settling regimes for individual particles and sedimentation laws have been determined (Fierstein and Hildreth, 1992; Hildreth and Drake, 1992; Rose, 1993; Bonadonna et al., 1998). Bonadonna et al. (1998) showed that three breaks in slope can be identified in the thinning rates of tephra-fall deposits. While the most proximal change in slope is related to the

transition from column margin to umbrella cloud fallout (see data for Mt. Spurr in Fig. 5), the other two breaks in slopes are interpreted as resulting from the particles' settling regime changing as the plume disperses away from vent. This is a consequence of a decrease in the Reynolds number of the particles, which is mostly related to a decrease in particle grainsize (Rose, 1993), which leads to transitions in particle settling regimes from turbulent (lapilli range), to transitional (coarse ash range), and laminar (fine ash range).

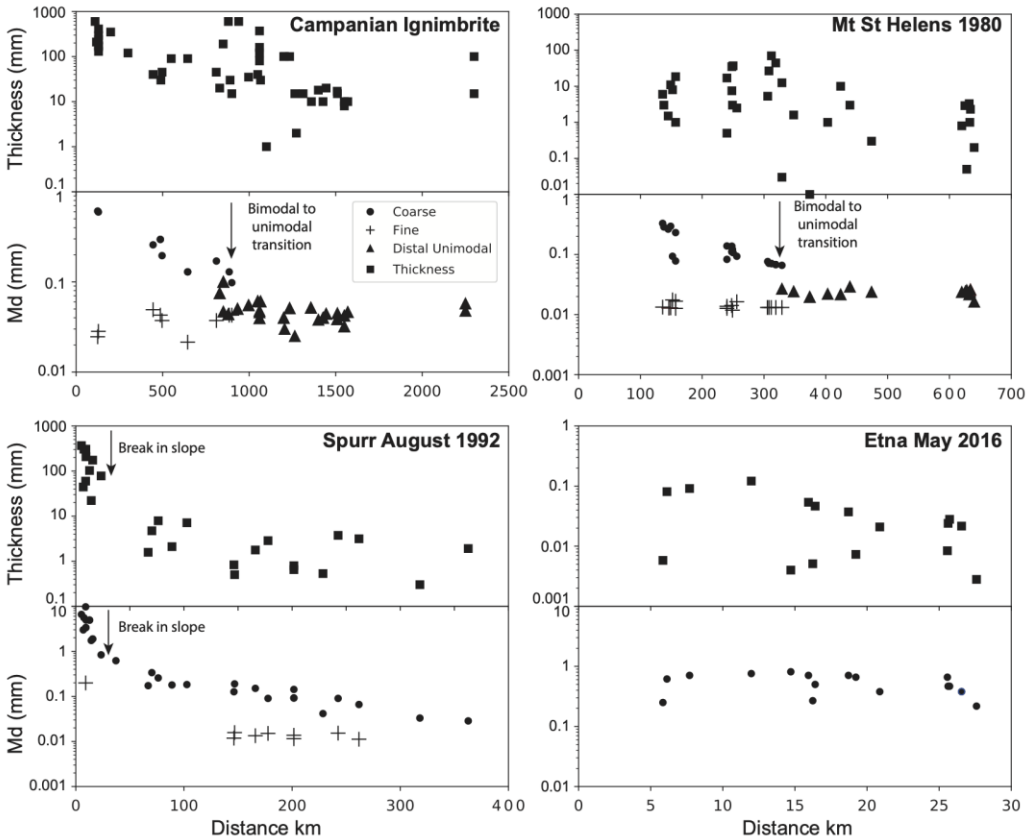

Figure 5. **Thickness and median grainsize are plotted versus distance for some key examples. For grainsize information, see Table S1 (see footnote 1). Thickness data are from Engwell et al. (2014), Sarna-Wojcicki et al. (1981), McGimsey et al. (2001), and Edwards et al. (2018).**

In many of the deposits compiled here, breaks in slopes are observed in the grainsize decay of the coarse trend with distance (Figs. 5 and S3), mimicking the changes identified in the thinning rates of fall deposits by Bonadonna et al. (1998). A steep decline of the grainsize decay is observed close to source, and a shallower decay is observed at greater distances: e.g., Askja D, Hekla 1947; Spurr, Tungurahua, Hekla 1991; Etna January 2011 (Figs. S3 and 5). The first break in slope occurs roughly at grainsizes around 10 mm (abrupt change) and the second sometimes identifiable break in slope is around 100 μm (more gradual change). Based on the theory of particle settling, these breaks in slopes can be related to the transition from turbulent to transitional and transitional to laminar settling regimes, respectively (Bursik et al., 1992; Ganser, 1993; Bagheri and Bonadonna, 2016). However, applying the particle settling scheme of Ganser (1993) to the August and September 1992 Spurr eruptions, Eychenne et al. (2017) demonstrated that in medial to distal areas, the shallow decay theoretically generated by particles falling in the laminar regime departs from the individual settling decay. This was also identified and discussed in other deposits (e.g., 2011 Cordón Caulle and 1980 Mount St. Helens eruptions; Durant et al., 2009; Rose and Durant, 2009; Bonadonna et al., 2015b). This implies that sedimentation in the depositional areas where grainsize and thickness show very little change with distance (i.e., the sedimentation of particles roughly below 100 μm) is controlled by a process other than individual settling.

Our compilation highlights that the shallow distal grainsize decay is the continuation of a shallow and fine trend in proximal and medial areas, which is composed of the fine subpopulations of bimodal deposits and the phreatomagmatic deposits (Fig. 3). The deposition of the fine subpopulation of bimodal deposits cannot be

caused by individual particle settling, given that at the same distances the particles settling individually comprise the coarse trend (Carey and Sigurdsson, 1986; Sparks et al., 1992; Eychenne et al., 2017). The questions raised by these observations are: (1) In proximal and medial areas of tephra-fall deposits, what are the processes controlling the sedimentation of fine ash (roughly below 100 μm) and generating the fine subpopulations of bimodal deposits and fine GSDs of phreatomagmatic deposits? (2) Are the same processes controlling the sedimentation of fine ash in distal areas and forming the distal unimodal deposits? These questions have been explored in the literature. It is anticipated that in proximal regions, both the high concentration of ash in the atmosphere and the wide range of particle sizes available can trigger aggregation (Brown et al., 2012) and other enhanced settling processes, such as hydrometeor formation (Durant et al., 2009; Van Eaton et al., 2015; Gudnason et al., 2017), deposition by gravitational instabilities (Carazzo and Jellinek, 2013; Manzella et al., 2015), and wake capture (Lovell and Rose, 1991). However, in more distal reaches, where volcanic plumes are more dilute and depleted in coarse material, processes triggered by particle interactions in highly concentrated mixtures, or by fine particle entrainment in the wake of coarse grains, are less likely to occur. Yet, even in distal ash clouds, fine ash particles can interact to form loose ash clusters (Sorem, 1982; Brown et al., 2012), and there is evidence of aggregate types changing from proximal (accretionary pellets) to distal (ash clusters) locations in individual fallout deposits (Brown et al., 2012). Additionally, atmospheric processes could be critical in controlling deposition of fine ash in distal areas. Vertical variations in atmospheric turbidity, humidity, and temperature can modulate the efficiency of aggregate and hydrometeor formation (Durant and Rose, 2009; Durant et al., 2009), while wind shear, convection, and orographic effects are also major controls on fine ash distribution and deposition (Eychenne et al., 2017; Poulidis et al., 2018). These different atmospheric processes, as well as the physico-chemical characteristics of the ash particles (i.e., density, texture, and shape), which strongly affect their transport and sedimentation behavior (Saxby et al., 2020), are all likely to make individual settling irrelevant for the deposition of fine ash.

To conclude, the distinctive coarse and fine grainsize decay observed in tephra-fall deposits provides evidence of the decoupled settling behavior between particles in the lapilli and coarse ash range and particles in the fine range. This leads to decoupled sedimentation behaviors in proximal/medial and distal areas. The deposition of fine ash itself does not result from a single ubiquitous process but is likely different in proximal and distal locations and sensitive to atmospheric conditions and particle characteristics.

Controls on Grainsize Decay Rates: Competition between Eruption Dynamics and Transport Processes

The patterns of grainsize decay in the coarse trend appear to be related to the eruption dynamics through the mass eruption rate (i.e., intensity), which is represented here by the maximum plume height above vent (Figs. 3 and 4). The decay in the coarse trend can be described in terms of (1) rate of decay (rate at which the grainsize decreases with distance from vent), and (2) position of the decay (grainsize found at a given distance from vent). This is evident when comparing eruptions with different intensities but parallel decay trends (Fig. 2E). In the case of magmatic eruptions, both are correlated with the plume height (Fig. 3). The correlation between decay rate and plume height means that the Md of tephra-fall deposits decreases more rapidly with distance from vent for high-intensity magmatic eruptions than low-intensity magmatic eruptions or phreatomagmatic eruptions (Fig. 3). The correlation between position of decay and plume height translates to the presence of coarser particles at a given distance (Fig. 4), and wider deposit extents, for more intense eruptions. Note for example the distance from vent at which the average grainsize of the deposits get below 100 μm in Figure 3.

The decay rate is theoretically related to the time it takes the particles to be transported and to settle through the atmosphere, and hence to particle transport and sedimentation mechanisms (Carey and Sparks, 1986; Pyle, 1989). These processes are mainly controlled by the type of settling mechanisms (individual or collective settling), the characteristics of the particles available for fallout in the plume (size, density, and shape), gravity current momentum in proximal areas, and wind velocity and other atmospheric processes. This latter dependence on atmospheric conditions explains the variability observed between decay rates within plume

height categories (Fig. 3). For example, the decay trend from the Pululagua eruption appears steeper than the rest of the coarse trend in Figure 3B and corresponds to a circular tephra-fall deposit (Volentik et al., 2010), which means that it was generated by a plume dominated by gravitational spreading and was not significantly affected by wind advection. The general increase in grainsize decay rate with increasing plume height (Figs. 2E and 3) could thus be explained by the larger effect of gravity spreading on the settling mechanisms of high intensity eruption plumes. Overall, the steep decay rates encountered in fall deposits from high-intensity eruptions reflect a high settling efficiency of particles in the plumes, which was previously demonstrated based on the lower proportion of far-traveled fine ash observed in high-intensity eruption plumes by satellite retrieval methods (Gouhier et al., 2019).

The position of the decay should be related to the grainsize distribution of the material available for fallout in the plume (specifically the maximum grainsize and the amount of fine ash) and the height of particle release (i.e., plume height). Indeed, the finer the grainsize distribution and the higher the particles released, the further they can be transported (Carey and Sparks, 1986; Pyle, 1989). The grainsize distribution of particles within the initial plume is controlled by the efficiency of fragmentation and the mass eruption rate. The higher the fragmentation efficiency, the higher the amount of fine ash produced (Cashman and Scheu, 2015), and the higher the mass eruption rate, the coarser the maximum tephra grainsize entrained and the higher the plume (Carey and Sparks, 1986). Fragmentation efficiency and mass eruption rate are strongly related, which explains why such a strong positive correlation between the position of decay and the maximum plume height above vent is observed in our data (Figs. 3 and 4).

To conclude, the patterns of grainsize decay are controlled by both transport mechanisms and source processes (i.e., the eruption dynamics, e.g., fragmentation, mass eruption rate, and height of particle release). The competition between transport and source processes controls the spatial grainsize variations in tephra-fall deposits.

Implications for Ash Transport in Distal Reaches

We demonstrate that tephra-fall deposits in distal areas show characteristic grainsize variations, regardless of eruption dynamics, whereby grainsize distributions are unimodal and show no change in Md with distance from vent (Figs. 2 and 3). This has been documented in deposits from large explosive eruptions such as the Campanian Ignimbrite, the Mazama, and Tambora 1815 eruptions (Kandlbauer et al., 2013; Engwell et al., 2014; Engwell and Eychenne, 2016; Buckland et al., 2020). We also show that the median grainsize in distal fall deposits, and the distance at which a deposit can be considered to be distal, vary among case studies and are strongly correlated to eruption intensity (Figs. 3 and 4). Most tephra deposits from eruptions with smaller (<10 km) plume heights extend less than 60 km from vent and never see their median grainsizes become constant or go below a value of 100 μm, apart from the January 2011 Etna eruption, which reaches a clear plateau at a Md value of 115 μm between 60 km and 100 km from vent (Fig. 3D). Deposits from eruptions with moderate plume heights (10– 20 km) plateau between 100 km and 300 km from vent, at Md values of between 100 μm and 50 μm (Fig. 3C). In eruptions with large plume heights (20–30 km), the distal deposit behavior is observed 200–500 km from vent at Md values of <50 μm (Fig. 3B), while for eruption deposits from very large plumes (>30 km), the transition is observed beyond 600 km from vent, at Md values of <50 μm (Fig. 3A).

The first implication of these findings is that, based on this grainsize pattern, it is possible to use objective and systematic criteria to identify "distal" areas of tephra-fall deposits. Indeed, the term "distal" is used ubiquitously in the description of volcanic deposits; however, it is rarely described in a quantitative way. We propose that the term "distal" be used where the grainsize of ash plateaus. The use of our criteria will allow fall deposits to be compared more effectively and better interpretation of the dispersion and sedimentation processes in play.

Our analyses of a comprehensive suite of fall deposits reinforce the previously reported observation that in distal areas, particles do not settle as individual particles due to their small sizes (<100 μm). Distal deposits represent

what is left in the plume after particles that settle according to their terminal velocities have already been deposited. Given that distal plumes have rather low concentrations, fine ash must reach the ground in distal areas because they are coupled to atmospheric flows (Eychenne et al., 2017; Poulidis et al., 2018, 2021) or due to loose aggregation (Brown et al., 2012). Quantifying the contribution of these processes in distal settling is challenging. But our data demonstrate a relation between the median grainsize of distal deposits and the eruption intensity (Fig. 3), which shows that eruption characteristics are key in controlling ash sedimentation in distal reaches. In distal deposits from low-intensity eruptions (plume height of <10 km), the absence of fine ash in high amounts at the source means that a plateau in grainsize is rarely seen, and when it occurs, it is in the coarse ash-size range (Md of ~100 μm). The contrasting grainsizes observed in distal deposits from eruptions with plume heights of >30 km above vent, compared to plume heights between 20 km and 30 km (40 and 25 μm, respectively; Fig. 3), could be predominantly controlled by the shape and textural properties of the grains (Riley et al., 2003; Saxby et al., 2018). Indeed, eruptions with plume heights of >30 km have extremely high intensities and tend to fragment highly vesicular magma and generate ash dominated by extreme shapes such as platy glass shards (Rose and Chesner, 1987; Engwell et al., 2014). These particles have low terminal velocities (Saxby et al., 2020), which means that 40 μm particles may be roughly aerodynamically equivalent to 25 μm particles with more standard shapes. This would lead to a relatively coarse grainsize threshold (~40 μm), below which individual settling becomes irrelevant, and to relatively coarse-grained distal deposits.

The major implication of these results is that processes not yet well understood control the dispersion and sedimentation of fine ash in distal reaches, and consequently the amount of fine ash that remains suspended in the atmosphere, where it is capable of traveling great distances. Far-traveled ash is a critical hazard in volcanology because of the severe impacts it has on (1) aviation, with disruption to air traffic and the potential for substantial economic loss (Budd et al., 2011), and (2) air quality, with potential adverse health effects (Horwell and Baxter, 2006; Carlsen et al., 2015) even at distances from vent of >1000 km (Balsa et al., 2016). There is discussion in the volcanology community about the size and amount of ash that reaches great distances, which varies depending on the records used, and in particular how information from tephra-fall deposits, satellite ash retrievals, and cryptotephra can be used together (Stevenson et al., 2015; Cashman and Rust, 2020; Gouhier et al., 2019). Deposit and cryptotephra records report coarser grainsizes than satellite data at the same distances from vent (Stevenson et al., 2015). The discrepancy between what is measured in the atmosphere and what is measured on the ground is difficult to resolve, given the fundamental differences in measurement methods and the limits of satellite ash-retrieval techniques (Stevenson et al., 2015). Here, we suggest using the constant and ubiquitous grainsizes observed in distal deposits as a benchmark to refine satellite ash-retrieval methods. As mentioned before, deposits and cryptotephra do not describe the same portion of the drifting ash plume, and we can suppose that cryptotephra are the continuation of distal tephra-fall deposits. The grainsizes measured in these two records should be carefully compared, as has been done in a few cases (Stevenson et al., 2015; Cashman and Rust, 2020), to understand the behavior of dilute ash clouds in ultra-distal reaches.

Implications for the Use of Tephra-Fall Deposit Records

Tephra-fall deposit records are used to interpret the dynamics (magnitude and intensity) of volcanic eruptions, specifically past eruptions that were not witnessed (e.g., Walker, 1973; Pyle, 1989; Bonadonna and Costa, 2013). They are also widely used as benchmarks for validating numerical models of tephra transport and deposition (e.g., Bonadonna et al., 2005; Folch et al., 2010; Woodhouse et al., 2013). These different applications have predominantly relied on thickness data and on trends of thickness variations with distance. When tephra thickness versus distance variations are compared to grainsize decays with distance, very similar trends are observed (i.e., steep decline in both grainsize and thickness close to source, with a levelling out at greater distances; Fig. 5). In most examples, the magnitude of change in grainsize over the extent of a deposit is comparable to that of tephra thickness. For a given eruption, the variability in grainsize at a given distance from source is considerably less than the variability in thickness (Fig. 5). Analysis of thickness and grainsize

information from the Campanian Ignimbrite eruption showed that higher thickness variability was related to depositional environment and secondary processes such as deposit remobilization and sedimentation (Engwell et al., 2014), with a comparatively smaller effect on deposit grainsize. Grainsize decay trends are excellent indicators of tephra transport and sedimentation processes. We thus argue that grainsize data provide a robust parameter for validating numerical model results, and that thickness and grainsize trends should be used conjointly.

CONCLUSIONS

We present an unprecedented data set compiling grainsize information for 56 tephra-fall deposits. This data set allows the inter-comparison of grainsize characteristics of fall deposits generated by eruptions of low to high intensities and magnitudes.

We highlight that fall deposits can show scattered or ubiquitous grainsize bimodality or unimodality. We demonstrate that deposits dominated by bimodal GSDs result from a high fine ash content at the source and enhanced deposition processes, while deposits displaying scattered subordinate bimodal GSDs result from local enhanced fine ash deposition processes.

We identified universal grainsize trends with distance from vent, whereby all tephra-fall deposits contribute to one of two distinct trends of grainsize decay: a coarse trend decreasing with distance from vent and a fine trend showing little change with distance. Both trends converge with distance in distal regions, where they reach a plateau of constant grainsize. These decoupled coarse and fine trends result from particle size-dependent contrasting sedimentation behaviors. In the lapilli and coarse ash size range, tephra sedimentation is dominated by individual particle settling at terminal fall velocity. In the fine ash size range, a combination of mechanisms is in play, from aggregation and other collective settlings to particle coupling with atmospheric flows. The contribution and relevance of these different processes are difficult to quantify, but we show that they do not have a particle size fractionation effect with distance from vent for particles sub ~100 microns. This leads to constant grainsizes in distal reaches of fall deposits, due to a depletion of the plume in particles capable of settling individually at such distances from vent.

We demonstrate that a correlation exists between plume height and grainsize decay in the coarse trend. This translates into larger Md at a given distance from vent for increasing eruption intensities and suggests that fragmentation and eruption dynamics at the vent (mass eruption rate) explain most of the variability among fall deposits from eruptions of different sizes, which overprints the effects of transport processes.

Our findings have implications for understanding the behavior of far-traveled volcanic ash, which is a major hazard that impacts aviation and health, and for improving the usage of tephra-fall deposit records. Further work is needed on employing records of observable tephra-fall deposit and cryptotephra to decipher the dispersion and sedimentation of volcanic ash at great distances from vent. We propose greater use of grainsize distribution data in addition to maximum grainsize and thickness data for interpreting deposits in terms of eruption dynamics and for validating numerical models of tephra transport and deposition.

ACKNOWLEDGMENTS

J. Eychenne acknowledges funding through the European Commission Marie Curie fellowship program, the French Institute for Sustainable Development (IRD), and the University Clermont-Auvergne I-Site CAP20-25 program, which all contributed to support this work. S.L. Engwell was supported by the Global Geological Risk Research Platform of the British Geological Survey NC-ODA grant NE/ R000069/1: Geoscience for Sustainable Futures and the European Union's Horizon 2020 project EUROVOLC (grant agreement no. 731070) and publishes with permission of the CEO of the British Geological Survey. Both authors thank all of the volcanologists who contributed to this work by sharing raw grainsize data: C. Bonadonna, A. Durant, K. Fontijn, B. Houghton, J. Kandlbauer, R. McGimsey, and K. Tsunematsu. We are particularly grateful to C.

Bonadonna and B. Houghton for sharing unpublished grainsize data with us. We thank editor Michael Ort, reviewer Costanza Bonadonna, Julia Crummy, and an anonymous reviewer for their constructive comments. This is Laboratory of Excellence ClerVolc contribution no. 556.

REFERENCES CITED

Alidibirov, M., and Dingwell, D.B., 1996, Magma fragmentation by rapid decompression: Nature, v. 380, no. 6570, p. 146–148, https://doi.org/10.1038/380146a0.

Aubry, T.J., Engwell, S., Bonadonna, C., Carazzo, G., Scollo, S., Van Eaton, A.R., Taylor, I.A., Jessop, D., Eychenne, J., Gouhier, M., Mastin, L.G., Wallace, K.L., Biass, S., Bursik, M., Grainger, R.G., Jellinek, A.M., and Schmidt, A., 2021, The Independent Volcanic Eruption Source Parameter Archive (IVESPA, version 1.0): A new observational database to support explosive eruptive column model validation and development: Journal of Volcanology and Geothermal Research, v. 417, https://doi.org/10.1016/j.jvolgeores.2021.107295.

Bagheri, G., and Bonadonna, C., 2016, On the drag of freely falling non-spherical particles: Powder Technology, v. 301, p. 526–544, https://doi.org/10.1016/j.powtec.2016.06.015.

Bagheri, G., Rossi, E., Biass, S., and Bonadonna, C., 2016, Timing and nature of volcanic particle clusters based on field and numerical investigations: Journal of Volcanology and Geothermal Research, v. 327, p. 520–530, https://doi.org/10.1016/j.jvolgeores.2016.09.009.

Balsa, A.I., Caffera, M., and Bloomfield, J., 2016, Exposures to particulate matter from the eruptions of the Puyehue volcano and birth outcomes in Montevideo, Uruguay: Environmental Health Perspectives, v. 124, no. 11, p. 1816–1822, https://doi.org/10.1289/EHP235.

Baxter, P.J., Ing, R., Falk, H., French, J., Stein, G.F., Bernstein, R.S., Merchant, J.A., and Allard, J., 1981, Mount St. Helens eruptions, May 18 to June 12, 1980: An overview of the acute health impact: Journal of the American Medical Association, v. 246, no. 22, p. 2585–2589, https://doi.org/10.1001/jama.1981.03320220035021.

Baxter, P.J., Searl, A.S., Cowie, H.A., Jarvis, D., and Horwell, C.J., 2014, Chapter 22: Evaluating the respiratory health risks of volcanic ash at the eruption of the Soufrière Hills Volcano, Montserrat, 1995 to 2010, *in* Wadge, G. Robertson, R.W.A., and Voight, B., eds., The Eruption of Soufrière Hills Volcano, Montserrat from 2000 to 2010: Geological Society, London, Memoir 39, no. 1, p. 407–425.

Beckett, F.M., Witham, C.S., Hort, M.C., Stevenson, J.A., Bonadonna, C., and Millington, S. C., 2015, Sensitivity of dispersion model forecasts of volcanic ash clouds to the physical characteristics of the particles: Journal of Geophysical Research: Atmospheres, p. 11,636–11,652.

Bellotti, F., Capra, L., Sarocchi, D., and D'Antonio, M., 2010, Geostatistics and multivariate analysis as a tool to characterize volcaniclastic deposits: Application to Nevado de Toluca volcano, Mexico: Journal of Volcanology and Geothermal Research, v. 191, no. 1–2, p. 117–128, https://doi.org/10.1016/j.jvolgeores.2010.01.005.

Bonadonna, C., and Costa, A., 2013, Plume height, volume, and classification of explosive volcanic eruptions based on the Weibull function: Bulletin of Volcanology, v. 75, no. 8, p. 1–19, https://doi.org/10.1007/s00445-013-0742-1.

Bonadonna, C., and Houghton, B.F., 2005, Total grain-size distribution and volume of tephra-fall deposits: Bulletin of Volcanology, v. 67, no. 5, p. 441–456, https://doi.org/10.1007/s00445-004-0386-2.

Bonadonna, C., Biass, S., and Costa, A., 2015a, Physical characterization of explosive volcanic eruptions based on tephra deposits: Propagation of uncertainties and sensitivity analysis: Journal of Volcanology and Geothermal Research, v. 296, p. 80–100, https://doi.org/10.1016/j.jvolgeores.2015.03.009.

Bonadonna, C., Cioni, R., Pistolesi, M., Elissondo, M., and Baumann, V., 2015b, Sedimentation of long-lasting wind-affected volcanic plumes: The example of the 2011 rhyolitic Cordón Caulle eruption, Chile: Bulletin of Volcanology, v. 77, no. 2, p. 1–19, https://doi.org/10.1007/s00445-015-0900-8.

Bonadonna, C., Costa, A., Folch, A., and Koyaguchi, T., 2015c, Tephra dispersal and sedimentation, *in* Sigurdsson, H., ed., The Encyclopedia of Volcanoes: Elsevier, p. 587–597, https://doi.org/10.1016/B978-0-12-385938-9.00033-X.

Bonadonna, C., Ernst, G.G.J., and Sparks, R.S.J., 1998, Thickness variations and volume estimates of tephra fall deposits: The importance of particle Reynolds number: Journal of Volcanology and Geothermal Research, v. 81, no. 3–4, p. 173–187, https://doi.org/10.1016/S0377-0273(98)00007-9.

Bonadonna, C., Macedonio, G., and Sparks, R.S.J., 2002a, Numerical modelling of tephra fallout associated with dome collapses and Vulcanian explosions: Application to hazard assessment on Montserrat, *in* Druitt, T.H., and Kokelaar, B.P., eds., 2002, The Eruption of Soufrière Hills Volcano, Montserrat, from 1995 to 1999: Geological Society, London, Memoir 21, p. 517–537.

Bonadonna, C., Mayberry, G.C., Calder, E.S., Sparks, R.S.J., Choux, C., Jackson, P., Lejeune, A.M., Loughlin, S.C., Norton, G.E., Rose, W.I., Ryan, G., and Young, S.R., 2002b, Tephra fallout in the eruption of Soufriere Hills Volcano, Montserrat *in* Druitt, T.H., and Kokelaar, B.P., eds., 2002, The Eruption of Soufrière Hills Volcano, Montserrat, from 1995 to 1999: Geological Society, London, Memoir 21, no. 1, p. 483–516.

Bonadonna, C., Phillips, J.C., and Houghton, B.F., 2005, Modeling tephra sedimentation from a Ruapehu weak plume eruption: Journal of Geophysical Research: Solid Earth, v. 110, no. B8, B08209.

Bonadonna, C., Genco, R., Gouhier, M., Pistolesi, M., Cioni, R., Alfano, F., Hoskuldsson, A., and Ripepe, M., 2011, Tephra sedimentation during the 2010 Eyjafjallajökull eruption (Iceland) from deposit, radar, and satellite observations: Journal of Geophysical Research: Solid Earth, v. 116, no. B12, B12202, https://doi.org/10.1029/2011JB008462.

Brazier, S., Davis, A.N., Sigurdsson, H., and Sparks, R.S.J., 1982, Fall-out and deposition of volcanic ash during the 1979 explosive eruption of the Soufrière of St. Vincent: Journal of Volcanology and Geothermal Research, v. 14, no. 3–4, p. 335–359, https://doi.org/10.1016/0377-0273(82)90069-5.

Brazier, S., Sparks, R.S.J., Carey, S.N., Sigurdsson, H., and Westgate, J.A., 1983, Bimodal grain size distribution and secondary thickening in air-fall ash layers: Nature, v. 301, p. 115–119, https://doi.org/10.1038/301115a0.

Brown, R.J., Bonadonna, C., and Durant, A.J., 2012, A review of volcanic ash aggregation: Physics and Chemistry of the Earth, v. 45–46, p. 65–78.

Buckland, H.M., Cashman, K.V., Engwell, S.L., and Rust, A.C., 2020, Sources of uncertainty in the Mazama isopachs and the implications for interpreting distal tephra deposits from large magnitude eruptions: Bulletin of Volcanology, v. 82, no. 3, p. 23, https://doi.org/10.1007/s00445-020-1362-1.

Buckland, H.M., Saxby, J., Roche, M., Meredith, P., Rust, A.C., Cashman, K.V., and Engwell, S.L., 2021, Measuring the size of non-spherical particles and the implications for grain size analysis in volcanology: Journal of Volcanology and Geothermal Research, v. 415, https:// doi.org/10.1016/j.jvolgeores.2021.107257.

Budd, L., Griggs, S., Howarth, D., and Ison, S., 2011, A fiasco of volcanic proportions? Eyjafjallajökull and the closure of European airspace: Mobilities, v. 6, no. 1, p. 31–40, https://doi.org/10.1080/17450101.2011.532650.

Burden, R.E., Phillips, J.C., and Hincks, T.K., 2011, Estimating volcanic plume heights from depositional clast size: Journal of Geophysical Research: Solid Earth, v. 116, no. B11206, https://doi.org/10.1029/2011JB008548.

Bursik, M.I., Sparks, R.S.J., Gilbert, J.S., and Carey, S.N., 1992, Sedimentation of tephra by volcanic plumes: I. Theory and its comparison with a study of the Fogo A Plinian deposit, Sao Miguel (Azores): Bulletin of Volcanology, v. 54, no. 4, p. 329–344, https://doi.org/10.1007/BF00301486.

Caballero, L., Sarocchi, D., Soto, E., and Borselli, L., 2014, Rheological changes induced by clast fragmentation

in debris flows: Journal of Geophysical Research: Earth Surface, v. 119, no. 9, https://doi.org/10.1002/2013JF002942.

Carazzo, G., and Jellinek, A.M., 2013, Particle sedimentation and diffusive convection in volcanic ash-clouds: Journal of Geophysical Research: Solid Earth, v. 118, no. 4,p. 1420–1437, https://doi.org/10.1002/jgrb.50155.

Carey, S., and Sigurdsson, H., 1986, The 1982 eruptions of El Chichon volcano, Mexico (2): Observations and nu- merical modelling of tephra-fall distribution: Bulletin of Volcanology, v. 48, p. 127–141, https://doi.org/10.1007/BF01046547.

Carey, S., and Sigurdsson, H., 1989, The intensity of Plinian eruptions: Bulletin of Volcanology, v. 51, no. 1, p. 28– 40, https://doi.org/10.1007/BF01086759.

Carey, S., and Sparks, R.S.J., 1986, Quantitative models of the fallout and dispersal of tephra from volcanic eruption columns: Bulletin of Volcanology, v. 48, no. 2, p. 109–125, https://doi.org/10.1007/BF01046546.

Carey, S.N., and Sigurdsson, H., 1982, Influence of particle aggregation on deposition of distal tephra from the May 18, 1980, eruption of Mount St. Helens volcano: Journal of Geophysical Research: Solid Earth, v. 87, no. B8, p. 7061–7072, https://doi.org/10.1029/JB087iB08p07061.

Carlsen, H.K., Gislason, T., Forsberg, B., Meister, K., Thorsteinsson, T., Jóhannsson, T., Finnbjornsdottir, R., and Oudin, A., 2015, Emergency hospital visits in association with volcanic ash, dust storms and other sources of ambient particles: A time-series study in Reykjavík, Iceland: International Journal of Environmental Research and Public Health, v. 12, no. 4, p. 4047–4059, https://doi.org/10.3390/ijerph120404047.

Cashman, K.V., and Rust, A.C., 2020, Far-travelled ash in past and future eruptions: Combining tephrochronology with volcanic studies: Journal of Quaternary Science, v. 35, p. 11–22, https://doi.org/10.1002/jqs.3159.

Cashman, K.V., and Scheu, B., 2015, Magmatic fragmentation, *in* Sigurdsson, H., ed., The Encyclopedia of Volcanoes (2nd edition): Cambridge, Massachussetts, Academic Press, p. 459–471, https://doi.org/10.1016/B978-0-12-385938-9.00025-0.

Costa, A., Macedonio, G., and Folch, A., 2006, A three-dimensional Eulerian model for transport and deposition of volcanic ashes: Earth and Planetary Science Letters, v. 241, no. 3–4, p. 634–647, https://doi.org/10.1016/j.epsl.2005.11.019.

Costa, A., Folch, A., and Macedonio, G., 2010, A model for wet aggregation of ash particles in volcanic plumes and clouds: 1. Theoretical formulation: Journal of Geophysical Research: Solid Earth, v. 115, no. B9, https://doi.org/10.1029/2009JB007175.

Costa, A., Pioli, L., and Bonadonna, C., 2016, Assessing tephra total grain-size distribution: Insights from field data analysis: Earth and Planetary Science Letters, v. 443,p. 90–107, https://doi.org/10.1016/j.epsl.2016.02.040.

Del Bello, E., Taddeucci, J., de' Michieli Vitturi, M., Scarlato, P., Andronico, D., Scollo, S., Kueppers, U., and Ricci, T., 2017, Effect of particle volume fraction on the settling velocity of volcanic ash particles: Insights from joint experimental and numerical simulations: Scientific Reports, v. 7, https://doi.org/10.1038/srep39620.

Deligne, N. I., 2021, Mass eruption rate, column height, and duration dataset for volcanic eruptions: GNS Science Report, 20 p., https://doi.org/10.21420/P18W-7674.

Dellino, P., Gudmundsson, M.T., Larsen, G., Mele, D., Stevenson, J.A., Thordarson, T., and Zimanowski, B., 2012, Ash from the Eyjafjallajökull eruption (Iceland): Fragmentation processes and aerodynamic behavior: Journal of Geophysical Research: Solid Earth, v. 117, no. B00C04.

Di Muro, A., Rosi, M., Aguilera, E., Barbieri, R., Massa, G., Mundula, F., and Pieri, F., 2008, Transport and sedimentation dynamics of transitional explosive eruption columns: The example of the 800 BP Quilotoa Plinian eruption (Ecuador): Journal of Volcanology and Geothermal Research, v. 174, no. 4, p. 307–324, https://doi.org/10.1016/j.jvolgeores.2008.03.002.

Durant, A.J., and Rose, W.I., 2009, Sedimentological constraints on hydrometeor-enhanced particle deposition: 1992 eruptions of Crater Peak, Alaska: Journal of Volcanology and Geothermal Research, v. 186, no. 1–2, p. 40–59, https://doi.org/10.1016/j.jvolgeores.2009.02.004.

Durant, A.J., Rose, W.I., Sarna-Wojcicki, A.M., Carey, S., and Volentik, A.C.M., 2009, Hydrometeor-enhanced tephra sedimentation: Constraints from the 18 May 1980 eruption of Mount St. Helens: Journal of Geophysical Research: Solid Earth, v. 114, no. B3, https:// doi.org/10.1029/2008JB005756.

Edwards, M.J., Pioli, L., Andronico, D., Scollo, S., Ferrari, F., and Cristaldi, A., 2018, Shallow factors controlling the explosivity of basaltic magmas: The 17–25 May 2016 eruption of Etna Volcano (Italy): Journal of Volcanology and Geothermal Research,v. 357, p. 425–436, https://doi.org/10.1016/j.jvolgeores.2018.05.015.

Engwell, S., and Eychenne, J., 2016, Chapter 4: Contribution of fine ash to the atmosphere from plumes associated with pyroclastic density currents, *in* Cashman, K., Ricketts, H., Rust, A., and Watson, M., eds., Volcanic Ash: Hazard Observation: Elsevier, p. 67–85, https://doi.org/10.1016/B978-0-08-100405-0.00007-0.

Engwell, S.L., Sparks, R.S.J., and Carey, S., 2014, Physical characteristics of tephra layers in the deep sea realm: The Campanian Ignimbrite eruption, *in* Austin, W.E.N., Abbott, P.M., Davies, S.M., Pearce, N.J.G., and Wastegärd, S., eds., Marine Tephrochronology: Geological Society, London, Special Publication, v. 398, p. 47–64, https://doi.org/10.1144/SP398.7.

Eychenne, J., Le Pennec, J.-L., Troncoso, L., Gouhier, M., and Nedelec, J.-M., 2012, Causes and consequences of bimodal grain-size distribution of tephra fall deposited during the August 2006 Tungurahua eruption (Ecuador): Bulletin of Volcanology, v. 74, no. 1, p. 187–205, https://doi.org/10.1007/s00445-011-0517-5.

Eychenne, J., Cashman, K.V., Rust, A.C., and Durant, A., 2015, Impact of the lateral blast on the spatial pattern and grain size characteristics of the May 18, 1980 Mount St. Helens fallout deposit: Journal of Geophysical Research: Solid Earth, v. 120, p. 6018–6038, https:// doi.org/10.1002/2015JB012116.

Eychenne, J., Rust, A.C., Cashman, K.V., and Wobrock, W., 2017, Distal enhanced sedimentation from volcanic plumes: Insights from the secondary mass maxima in the 1992 Mount Spurr fallout deposits: Journal of Geophysical Research: Solid Earth, v. 122, no. 10, p. 7679–7697, https://doi.org/10.1002/2017JB014412.

Fierstein, J., and Hildreth, W., 1992, The Plinian eruptions of 1912 at Novarupta, Katmai National Park, Alaska: Bulletin of Volcanology, v. 54, no. 8, p. 646–684, https://doi.org/10.1007/BF00430778.

Fisher, R., 1964, Maximum size, median diameter, and sorting of tephra: Journal of Geophysical Research, v. 69,p. 341–355, https://doi.org/10.1029/JZ069i002p00341. Folch, A., Costa, A., Durant, A., and Macedonio, G., 2010, A model for wet aggregation of ash particles in volcanic plumes and clouds: 2. Model application: Journal of Geophysical Research: Solid Earth, v. 115, no. B9, https://doi.org/10.1029/2009JB007176.

Ganser, G.H., 1993, A rational approach to drag prediction of spherical and nonspherical particles: Powder Technology, v. 77, no. 2, p. 143–152, https://doi.org/10.1016/0032-5910(93)80051-B.

Girault, F., Carazzo, G., Tait, S., Ferrucci, F., and Kaminski, É., 2014, The effect of total grain-size distribution on the dynamics of turbulent volcanic plumes: Earth and Planetary Science Letters, v. 394, p. 124–134, https:// doi.org/10.1016/j.epsl.2014.03.021.

Gouhier, M., Eychenne, J., Azzaoui, N., Guillin, A., Deslandes, M., Poret, M., Costa, A., and Husson, P., 2019, Low efficiency of large volcanic eruptions in transporting very fine ash into the atmosphere: Scientific Reports, v. 9, no. 1, p. 1449, https://doi.org/10.1038/s41598-019-38595-7.

Gudnason, J., Thordarson, T., Houghton, B.F., and Larsen, G., 2017, The opening subplinian phase of the Hekla 1991 eruption: Properties of the tephra fall deposit: Bulletin of Volcanology, v. 79, no. 5, p. 34, https://doi.org/10.1007/s00445-017-1118-8.

Gudnason, J., Thordarson, T., Houghton, B.F., and Larsen, G., 2018, The 1845 Hekla eruption: Grain-size characteristics of a tephra layer: Journal of Volcanology and Geothermal Research, v. 350, p. 33–46, https://doi.org/10.1016/j.jvolgeores.2017.11.025.

Hildreth, W., and Drake, R.E., 1992, Volcan Quizapu, Chilean Andes: Bulletin of Volcanology, v. 54, p. 93–125, https://doi.org/10.1007/BF00278002.

Horwell, C., and Baxter, P., 2006, The respiratory health hazards of volcanic ash: A review for volcanic risk mitigation: Bulletin of Volcanology, v. 69, p. 1–24, https://doi.org/10.1007/s00445-006-0052-y.

Inman, D.L., 1952, Measures for describing the size distribution of sediments: Journal of Sedimentary Research,v. 22, p. 125–145.

Janebo, M.H., Houghton, B.F., Thordarson, T., Bonadonna, C., and Carey, R.J., 2018, Total grain-size distribution of four subplinian–Plinian tephras from Hekla volcano, Iceland: Implications for sedimentation dynamics and eruption source parameters: Journal of Volcanology and Geothermal Research, v. 357, p. 25–38, https://doi.org/10.1016/j.jvolgeores.2018.04.001.

Kandlbauer, J., Carey, S.N., and Sparks, R.S.J., 2013, The 1815 Tambora ash fall: Implications for transport and deposition of distal ash on land and in the deep sea: Bulletin of Volcanology, v. 75, no. 4, p. 1–11, https://doi.org/10.1007/s00445-013-0708-3.

Kueppers, U., Cimarelli, C., Hess, K.-U., Taddeucci, J., Wadsworth, F., and Dingwell, D., 2014, The thermal stability of Eyjafjallajokull ash versus turbine ingestion test sands: Journal of Applied Volcanology, v. 3, no. 1, p. 4, https://doi.org/10.1186/2191-5040-3-4.

Liu, E.J., Cashman, K.V., Beckett, F.M., Witham, C.S., Leadbetter, S.J., Hort, M.C., and Guðmundsson, S., 2014, Ash mists and brown snow: Remobilization of volcanic ash from recent Icelandic eruptions: Journal of Geophysical Research: Atmospheres, v. 119, no. 15,p. 9463–9480, https://doi.org/10.1002/2014JD021598.

Liu, E.J., Cashman, K.V., Rust, A.C., and Gislason, S.R., 2015, The role of bubbles in generating fine ash during hydromagmatic eruptions: Geology, v. 43, no. 3,p. 239–242, https://doi.org/10.1130/G36336.1.

Lovell, C.J., and Rose, C.W., 1991, Wake-capture effects observed in a comparison of methods to measure particle settling velocity beyond Stokes' Range: Journal of Sedimentary Research, v. 61, p. 575–582.

Maeno, F., Nakada, S., Yoshimoto, M., Shimano, T., Hokanishi, N., Zaennudin, A., and Iguchi, M., 2019, A sequence of a Plinian eruption preceded by dome destruction at Kelud volcano, Indonesia, on February 13, 2014, revealed from tephra fallout and pyroclastic density current deposits: Journal of Volcanology and Geothermal Research, v. 382, p. 24–41, https://doi.org/10.1016/j.jvolgeores.2017.03.002.

Mahony, S.H., Sparks, R.S.J., Wallace, L.M., Engwell, S.L., Scourse, E.M., Barnard, N.H., Kandlbauer, J., and Brown, S.K., 2016, Increased rates of large-magnitude explosive eruptions in Japan in the late Neogene and Quaternary: Geochemistry, Geophysics, Geosystems, v. 17, no. 7, p. 2467–2479, https://doi.org/10.1002/2016GC006362.

Manzella, I., Bonadonna, C., Phillips, J.C., and Monnard, H., 2015, The role of gravitational instabilities in deposition of volcanic ash: Geology, v. 43, p. 211–214, https:// doi.org/10.1130/G36252.1.

Mastin, L.G., Guffanti, M., Servranckx, R., Webley, P., Barsotti, S., Dean, K., Durant, A., Ewert, J.W., Neri,

A., Rose, W.I., Schneider, D., Siebert, L., Stunder, B., Swanson, G., Tupper, A., Volentik, A., and Waythomas, C.F., 2009, A multidisciplinary effort to assign realistic source parameters to models of volcanic ash-cloud transport and dispersion during eruptions: Journal of Volcanology and Geothermal Research, v. 186, no. 1–2,p.

10–21, https://doi.org/10.1016/j.jvolgeores.2009.01.008.

McGimsey, R.G., Neal, C.A., and Riley, C.M., 2001, Areal distribution, thickness, mass, volume and grainsize of tephra-fall deposits from the 1992 eruptions of Creater Peak vent, Mt. Spurr Volcano, Alaska: U.S. Geological Survey Open-File Report 01-370, 38 p.

Osman, S., Beckett, F., Rust, A., and Snee, E., 2020, Sensitivity of volcanic ash dispersion modelling to input grain size distribution based on hydromagmatic and magmatic deposits: Atmosphere, v. 11, no. 6, p. 567, https://doi.org/10.3390/atmos11060567.

Pedrazzi, D., Sunye-Puchol, I., Aguirre-Díaz, G., Costa, A., Smith, V.C., Poret, M., Dávila-Harris, P., Miggins, D.P., Hernández, W., and Gutiérrez, E., 2019, The Ilopango Tierra Blanca Joven (TBJ) eruption, El Salvador: Volcano-stratigraphy and physical characterization of the major Holocene event of Central America: Journal of Volcanology and Geothermal Research, v. 377, p. 81– 102, https://doi.org/10.1016/j.jvolgeores.2019.03.006.

Perrotta, A., and Scarpati, C., 2003, Volume partition between the Plinian and co-ignimbrite air fall deposits of the Campanian Ignimbrite eruption: Mineralogy and Petrology, v. 79, no. 1, p. 67–78, https://doi.org/10.1007/s00710-003-0002-8.

Pioli, L., Bonadonna, C., and Pistolesi, M., 2019, Reliability of total grain-size distribution of tephra deposits: Scientific Reports, v. 9, no. 1, 10006, https://doi.org/10.1038/s41598-019-46125-8.

Ponomareva, V., Portnyagin, M., and Davies, S.M., 2015, Tephra without borders: Far-reaching clues into past explosive eruptions: Frontiers of Earth Science, v. 3, 83. Poulidis, A.P., Phillips, J.C., Renfrew, I.A., Barclay, J., Hogg, A., Jenkins, S.F., Robertson, R., and Pyle, D.M., 2018, Meteorological controls on local and regional volcanic ash dispersal: Scientific Reports, v. 8, no. 1, 6873, https://doi.org/10.1038/s41598-018-24651-1.

Poulidis, A.P., Biass, S., Bagheri, G., Takemi, T., and Iguchi, M., 2021, Atmospheric vertical velocity—a crucial component in understanding proximal deposition of volcanic ash: Earth and Planetary Science Letters, v. 566, https://doi.org/10.1016/j.epsl.2021.116980

Pyle, D.M., 2000, Sizes of volcanic eruptions, *in* Sigurdsson, H., Houghton, B., Rymer, H., Stix, J., and McNutt, S., Encyclopedia of Volcanoes, Volume 1: Elsevier,p. 263–269.

Pyle, D.M., 1989, The thickness, volume and grainsize of tephra fall deposits: Bulletin of Volcanology, v. 51, p. 1–15, https://doi.org/10.1007/BF01086757.

Pyle, D.M., 1995, Mass and energy budgets of explosive volcanic eruption: Geophysical Research Letters, v. 22, no. 5, p. 563–566, https://doi.org/10.1029/95GL00052.

Riley, C.M., Rose, W.I., and Bluth, G.J.S., 2003, Quantitative shape measurements of distal volcanic ash: Journal of Geophysical Research: Solid Earth, v. 108, no. B10,p. 2504.

Rose, W., and Durant, A., 2009, Fine ash content of explosive eruptions: Journal of Volcanology and Geothermal Research, v. 186, p. 32–39, https://doi.org/10.1016/j.jvolgeores.2009.01.010.

Rose, W., Self, S., Murrow, P., Bonadonna, C., Durant, A., and Ernst, G., 2008, Nature and significance of small volume fall deposits at composite volcanoes: Insights from the October 14, 1974 Fuego eruption, Guatemala: Bulletin of Volcanology, v. 70, no. 9, p. 1043–1067, https://doi.org/10.1007/s00445-007-0187-5.

Rose, W.I., 1993, Comment on 'another look at the calculation of fallout tephra volumes' by Judy Fierstein and Manuel Nathenson: Bulletin of Volcanology, v. 55, no. 5, p. 372–374, https://doi.org/10.1007/BF00301148.

Rose, W.I., and Chesner, C.A., 1987, Dispersal of ash in the great Toba eruption, 75 ka: Geology, v. 15, no. 10, p. 913–917, https://doi.org/10.1130/0091-7613(1987)15<913:DOAITG>2.0.CO;2.

Rossi, E., Bonadonna, C., and Degruyter, W., 2019, A new strategy for the estimation of plume height from clast dispersal in various atmospheric and eruptive conditions: Earth and Planetary Science Letters, v. 505, p. 1–

12, https://doi.org/10.1016/j.epsl.2018.10.007.

Rust, A.C., and Cashman, K.V., 2011, Permeability controls on expansion and size distributions of pyroclasts: Journal of Geophysical Research: Solid Earth, v. 116, no. B11, B11202.

Sarna-Wojcicki, A., Shipley, S., Waitt, R.B., Dzurisin, D., and Wood, S., 1981, Aeral distribution, thickness, mass, volume and grain size of air-fall ash from the six major eruptions of 1980: U.S. Geological Survey Professional Paper, v. 1250, p. 577–600.

Saxby, J., Beckett, F., Cashman, K., Rust, A., and Tennant, E., 2018, The impact of particle shape on fall velocity: Implications for volcanic ash dispersion modelling: Journal of Volcanology and Geothermal Research, v. 362, p. 32– 48, https://doi.org/10.1016/j.jvolgeores.2018.08.006.

Saxby, J., Rust, A., Cashman, K., and Beckett, F., 2020, The importance of grain size and shape in controlling the dispersion of the Vedde cryptotephra: Journal of Quaternary Science, v. 35, no. 1–2, p. 175–185, https://doi.org/10.1002/jqs.3152.

Scasso, R.A., Corbella, H., and Tiberi, P., 1994, Sedimentological analysis of the tephra from the 12–15 August 1991 eruption of Hudson volcano: Bulletin of Volcanology, v. 56, no. 2, p. 121–132, https://doi.org/10.1007/BF00304107.

Scheidegger, K.F., Federman, A.N., and Tallman, A.M., 1982, Compositional heterogeneity of tephras from the 1980 eruptions of Mount St. Helens: Journal of Geophysical Research: Solid Earth, v. 87, no. B13, p. 10,861–10,881, https://doi.org/10.1029/JB087iB13p10861.

Sorem, R.K., 1982, Volcanic ash clusters: Tephra rafts and scavengers: Journal of Volcanology and Geothermal Research, v. 13, no. 1–2, p. 63–71, https://doi.org/10.1016/0377-0273(82)90019-1.

Sparks, R.S.J., and Huang, T.C., 1980, The volcanological significance of deep-sea ash layers associated with ignimbrites: Geological Magazine, v. 117, p. 425–436, https://doi.org/10.1017/S0016756800028533.

Sparks, R.S.J., Brazier, S., Huang, T.C., and Muerdter, D., 1983, Sedimentology of the Minoan deep-sea tephra layer in the Aegean and eastern Mediterranean: Marine Geology, v. 54, p. 131–167, https://doi.org/10.1016/0025-3227(83)90011-7.

Sparks, R.S.J., Bursik, M.I., Ablay, G.J., Thomas, R.M.E., and Carey, S.N., 1992, Sedimentation of tephra by volcanic plumes. Part 2: Controls on thickness and grain-size variations of tephra fall deposits: Bulletin of Volcanology, v. 54, no. 8, p. 685–695, https://doi.org/10.1007/BF00430779.

Stevenson, J.A., Millington, S.C., Beckett, F.M., Swindles, G.T., and Thordarson, T., 2015, Big grains go far: Reconciling tephrochronology with atmospheric measurements of volcanic ash: Atmospheric Measurement Techniques Discussions, v. 8, no. 1, p. 65–120, https:// doi.org/10.5194/amtd-8-65-2015.

Tadini, A., Roche, O., Samaniego, P., Guillin, A., Azzaoui, N., Gouhier, M., de' Michieli Vitturi, M., Pardini, F., Eychenne, J., Bernard, B., Hidalgo, S., and Le Pennec,

J. L., 2020, Quantifying the uncertainty of a coupled plume and tephra dispersal model: PLUME-MOM/HYSPLIT simulations applied to Andean Volcanoes: Journal of Geophysical Research: Solid Earth, v. 125, no. 2, https://doi.org/10.1029/2019JB018390.

Thorarinsson, S., 1954, The eruption of Hekla, 1947–1948, Part II 3. The tephra-fall from Hekla on March 29th, 1947: Visindafelag Islendinga, v. 68.

Van Eaton, A.R., Mastin, L.G., Herzog, M., Schwaiger, H.F., Schneider, D.J., Wallace, K.L., and Clarke, A.B., 2015, Hail formation triggers rapid ash aggregation in volcanic plumes: Nature Communications, v. 6, https://doi.org/10.1038/ncomms8860.

Vasseur, J., Wadsworth, F.B., Lavallée, Y., Hess, K.-U., and Dingwell, D.B., 2013, Volcanic sintering: Timescales

of viscous densification and strength recovery: Geophysical Research Letters, v. 40, no. 21, p. 5658–5664, https://doi.org/10.1002/2013GL058105.

Volentik, A.C.M., Bonadonna, C., Connor, C.B., Connor, L.J., and Rosi, M., 2010, Modeling tephra dispersal in absence of wind: Insights from the climactic phase of the 2450 BP Plinian eruption of Pululagua volcano (Ecuador): Journal of Volcanology and Geothermal Research, v. 193, no. 1, p. 117–136, https://doi.org/10.1016/j.jvolgeores.2010.03.011.

Walker, G., 1973, Explosive volcanic eruptions—a new classification scheme: Geologische Rundschau, v. 62, no. 2,p. 431–446, https://doi.org/10.1007/BF01840108. Walker, G.P.L., 1971, Grain-size characteristics of pyroclastic deposits: The Journal of Geology, v. 79, p. 696–714, https://doi.org/10.1086/627699.

Walker, G.P.L., 1981, Characteristics of two phreatoplinian ashes, and their water-flushed origin: Journal of Volcanology and Geothermal Research, v. 9, no. 4, p. 395– 407, https://doi.org/10.1016/0377-0273(81)90046-9.

Walker, G.P.L., Wilson, L., and Bowell, E.L.G., 1971, Explosive volcanic eruptions—I The rate of fall of pyroclasts: Geophysical Journal International, v. 22, no. 4, p. 377–383, https://doi.org/10.1111/j.1365-246X.1971.tb03607.x.

Watt, S.F.L., Pyle, D.M., Mather, T.A., Martin, R.S., and Matthews, N.E., 2009, Fallout and distribution of volcanic ash over Argentina following the May 2008 explosive eruption of Chaitén, Chile: Journal of Geophysical Research: Solid Earth, v. 114, no. B4, B04207, https://doi.org/10.1029/2008JB006219.

Watt, S.F.L., Gilbert, J.S., Folch, A., Phillips, J.C., and Cai, X.M., 2015, An example of enhanced tephra deposition driven by topographically induced atmospheric turbulence: Bulletin of Volcanology, v. 77, no. 5, p. 1–14, https://doi.org/10.1007/s00445-015-0927-x.

Wohletz, K.H., Sheridan, M.F., and Brown, W.K., 1989, Particle size distributions and the sequential fragmentation/transport theory applied to volcanic ash: Journal of Geophysical Research: Solid Earth, v. 94, no. B11, p. 15,703–15,721, https://doi.org/10.1029/JB094iB11p15703.

Woodhouse, M.J., Hogg, A.J., Phillips, J.C., and Sparks, R.S.J., 2013, Interaction between volcanic plumes and wind during the 2010 Eyjafjallajökull eruption, Iceland: Journal of Geophysical Research: Solid Earth, v. 118, no. 1, p. 92–109, https://doi.org/10.1029/2012JB009592.

TABLE 1: SUMMARY OF THE 56 TEPHRA FALL DEPOSITS STUDIED FOR GRAINSIZE. The references for the source of the grainsize data, and the magnitude and plume height information are in [ ] and listed in Supplementary Information. * Unpublished raw grainsize data from C. Bonadonna and B. Houghton.

Eruption/ Deposit ID	Volcano	Country	Date/ Deposit Name	Deposit category	Source grainsize data	Eruption Type	Magnitude		Max Plume Height above vent (km)	
Hverfjall phreato	Krafla	Iceland	2500 BP Hverfjall Fires (phreatomag. unit)	Unimodal	[1]	Phreatomagmatic	3.9	[1]	Unknown	
Taupo	Taupo	New Zealand	186AD	Unimodal	[2]	Magmatic	5.7	[2, 3]	37	[4]
Rungwe	Rungwe	Tanzania	4ka Rungwe Pumice	Unimodal	[5]	Magmatic	5.3	[5]	35	[5]
Huaynaputina	Huaynaputina	Peru	1600 stage-1	Unimodal	[6]	Magmatic	5.9	[7]	34.7	[7]
Quizapu	Quizapu	Chile	10-11 April 1932	Unimodal	[8]	Magmatic	5.8	[8]	32	[8]
ElChichon	El Chichon	Mexico	4 April 1982 (B+C)	Unimodal	[9]	Magmatic	4.9	[9]	32	[10]
Hekla 1947	Hekla	Iceland	1947	Unimodal	[11]	Magmatic	4.1	[11]	28.5	[11]
Askja D	Askja	Iceland	28-29 March 1875 Layer D	Unimodal	[12]	Magmatic	4.7	[13]	26	[13]
Kelud	Kelud	Indonesia	13 February 2014	Unimodal	[14]	Magmatic	4.6	[14]	26	[15]
Hekla 1104	Hekla	Iceland	1104	Unimodal	[16]	Magmatic	4.6	[17]	25	[17]
Hekla 1300	Hekla	Iceland	1300D opening phase	Unimodal	[16]	Magmatic	4.4	[17]	25	[17]
Pululagua	Pululagua	Ecuador	2450 BP - BF2 layer	Unimodal	[18]	Magmatic	4.4	[18]	23.8	[18]
Askja C1	Askja	Iceland	28-29 March 1875 Layer C1	Unimodal	[12, 13]	Phreatomagmatic	4.7	[13]	22.8	[13]
Cotopaxi L3	Cotopaxi	Ecuador	Layer 3	Unimodal	[19]	Magmatic	5.4	[20]	21	[20]
Cotopaxi L5	Cotopaxi	Ecuador	Layer 5	Unimodal	[19]	Magmatic	4.7	[20]	20	[20]
Grimsvötn	Grimsvotn	Iceland	21-22 May 2011	Unimodal	[21, 22]	Magmatic	4.9	[23]	18.3	[24, 25]
Hekla 1766	Hekla	Iceland	1766	Unimodal	[16]	Magmatic	3.9	[17]	18	[17]
Hekla 1693	Hekla	Iceland	1693	Unimodal	[16]	Magmatic	4.0	[17]	17	[17]
Eldgja	Eldgja	Iceland	Unit 7 (magmatic)	Unimodal	[26]	Magmatic	3.8	[26]	17	[26]
Hekla 1991	Hekla	Iceland	17-18 January 1991 opening phase	Unimodal	[27]	Magmatic	3.0	[27]	11.5	[28]
Spurr Sept	Mount Spurr	Alaska	16-17 September 1992	Unimodal	[29, 30]	Magmatic	3.6	[30]	10.6	[31]
Eyja 6 May	Eyjafjallajökull	Iceland	6 May 2010	Unimodal	[32-36]	Magmatic	2.9	[32]	8.2	[32]
Askja B	Askja	Iceland	28-29 March 1875 Layer B	Unimodal	[12]	Magmatic	3.0	[13]	8	[13]
Kirishima	Kirishima	Japan	26-27 January 2011 (unit 2)	Unimodal	[37]	Magmatic	2.8	[37]	7.08	[37, 38]
Eyja 5 May	Eyjafjallajökull	Iceland	5 May 2010	Unimodal	[32-36]	Magmatic	3.5	[32]	6	[32]
Etna 18-19 May 2016	Etna	Italy	18-19 May 2016	Unimodal	[39]	Magmatic	0.6	[39]	3.5	[39]
Eyja 4 May	Eyjafjallajökull	Iceland	4 May 2010	Unimodal	[32-36]	Magmatic	2.9	[32]	4	[32]
Etna 28 Oct 2002	Etna	Italy	28 October 2002	Unimodal	[40]	Magmatic	2.0	[40]	4.2	[40]
Etna 31 Oct 2002	Etna	Italy	31 October 2002	Unimodal	[40]	Magmatic	1.7	[40]	3.7	[40]
Etna 27 Oct 2002	Etna	Italy	27 October 2002	Unimodal	[40]	Magmatic	1.9	[40]	3.2	[40]
Etna Jan 2011	Etna	Italy	12-13 January 2011	Unimodal	[41]	Magmatic	1.2	[41]	6	[41,42]
Etna 21 May 2016	Etna	Italy	21 May 2016	Unimodal	[39]	Magmatic	-0.3	[39]	3	[39]

Etna 4 Nov 2002	Etna	Italy	4 November 2002	Unimodal	[41]	Magmatic	2.1	[40]	2.9	[40]
Etna July 2001	Etna	Italy	July 2001	Unimodal	[43]	Magmatic	2.2	[43]	1.68	[43]
Heimaey	Heimaey	Iceland	1 Feb 1973 (Scoria fall II)	Unimodal	[44]	Magmatic	NA	[44]	1	[44]
Aso 2004	Aso	Japan	14 January 2004	Unimodal	[45]	Phreatomagmatic	-2.5	[45]	0.8	[45]
Aso 2003	Aso	Japan	10 July 2003	Unimodal	[46]	Phreatomagmatic	-2.4	[46]	0.5	[46]
Reykjanes	Reykjanes	Iceland	CE1226 (medieval tephra)	Unimodal	[46]	Phreatomagmatic	4.0	[46]	Unknown	
Chaiten	Chaiten	Chile	6 May 2008	Unimodal *with scattered bimodal distributions*	[47, 48]	Magmatic	4.2	[48]	18.9	[49]
Spurr Aug	Mount Spurr	Alaska	18 August 1992	Unimodal *with scattered bimodal distributions*	[29, 30]	Magmatic	3.6	[30]	10.4	[31]
Eyja 14-16 April	Eyjafjallajökull	Iceland	14-16 April 2010	Unimodal *with scattered bimodal distributions*	[32-36]	Phreatomagmatic	4.0	[32]	8	[32]
Ruapehu	Ruapehu	New Zealand	17 June 1996	Unimodal *with scattered bimodal distributions*	[51]*	Magmatic	2.6	[50]	5.7	[51, 52]
Eyja 7 May	Eyjafjallajökull	Iceland	7 May 2010	Unimodal *with scattered bimodal distributions*	[32-36]	Magmatic	2.9	[32]	5	[32]
Hekla 1845	Hekla	Iceland	1845	Bimodal	[53]	Magmatic	4.0	[53]	30	[53]
Hudson	Cerro Hudson	Chile	12-15 August 1991	Bimodal	[54]	Magmatic	5.9	[53]	18	[55]
Tungurahua	Tungurahua	Ecuador	16 August 2006	Bimodal	[56]	Magmatic	3.6	[56, 57]	18	[56, 58]
Fuego	Fuego	Guatemala	14 October 1974	Bimodal	[59]	Magmatic	3.7	[59]	11	[59]
Montserrat	Soufriere Hills	Montserrat	26 September 1997	Bimodal	[60]	Magmatic	1.7	[50]	10.4	[60]
Mazama	Crater Lake	USA	7.7 ka Mazama	Bimodal *with distal unimodal distributions*	[61]	Magmatic	7.1	[62]	55	[63]
Campanian	Campi Flegrei	Italy	Campanian Plinian fall	Bimodal *with distal unimodal distributions*	[64]	Magmatic	6.3	[65]	44	[66]
Tambora	Tambora	Indonesia	1815 total Fallout	Bimodal *with distal unimodal distributions*	[67]	Magmatic	5.8	[68]	43	[68]
Pinatubo	Pinatubo	Philippines	15 June 1991	Bimodal *with distal unimodal distributions*	[69, 70]	Magmatic	5.8	[70]	38.3	[71]
Minoan	Santorini	Greece	3.5 ka Minoan	Bimodal *with distal unimodal distributions*	[72, 73]	Magmatic	6.6	[74]	38	[75]
MSH Yn	Mount St. Helens	USA	3.5 ka Yn	Bimodal *with distal unimodal distributions*	[61]	Magmatic	6.1	[63]	31	[63]

Glacier Peak	Glacier Peak	USA	11.2 ka Chiwawa ash (Layer B)	Bimodal *with distal unimodal distributions*	[61]	Magmatic	5.8	[63]	31	[63]
MSH 1980	Mount St. Helens	USA	18 May 1980	Bimodal *with distal unimodal distributions*	[76, 77]	Magmatic	4.7	[78]	27.5	[79-81]